MASTER'S THESIS

Nanomaterials based on reduced graphene oxide: radiolytic synthesis and application in the field of energy storage

Author
Liran Hu

Supervisor
Prof. Samy Remita

Institut de Chimie Physique (ICP)
UMR 8000 CNRS

Table of Contents

Abstract

Graphene and its composites are of primary importance, particularly in the field of energy. Numerous bottom-up and top-down methods have been proposed in the literature to produce these materials with enhanced physicochemical properties. Recently, an innovative and green methodology was developed at Institut de Chimie Physique based on ionizing radiation, allowing the quantitative synthesis of graphene oxide-based materials. To extend this strategy for the preparation of hybrid nanomaterials, the objective of this work is the one-pot synthesis of nanocomposites composed of reduced graphene oxide – gold nanoparticles (rGO-AuNPs) via gamma ray-induced radiolytic reduction. UV-Vis Absorption Spectroscopy, Fourier Transform Infrared Spectroscopy, Raman Spectroscopy and X-ray Photoemission Spectroscopy were utilized to comprehensively evaluate the reduction degree of graphene oxide and the formation of gold nanoparticles. Atomic Force Microscopy and Scanning Electron Microscopy were employed to obtain the morphological and topographical information on synthesized nanocomposites. Thermal properties were investigated by Thermogravimetric Analysis and electrical properties were investigated using Cyclic Voltammetry and Potentiostatic Charge and Discharge method. The results demonstrated the successful reduction of both graphene oxide and gold ions through the drastic transformation of oxygen-containing functional groups and the formation of gold nanoparticles. Electrical characterization results highlighted excellent electrical properties and potential for supercapacitance application.

Résumé

Le graphène et ses composites revêtent une importance primordiale, en particulier dans le domaine de l'énergie. De nombreuses méthodes ascendantes et descendantes ont été proposées dans la littérature pour produire ces matériaux avec des propriétés physico-chimiques améliorées. Récemment, une méthodologie innovante et écologique a été développée à l'Institut de Chimie Physique, basée sur les rayonnements ionisants, permettant la synthèse quantitative de matériaux à base d'oxyde de graphène. Pour étendre cette stratégie à la préparation de nanomatériaux hybrides, l'objectif de ce travail est la synthèse en une seule étape de nanocomposites composés d'oxyde de graphène réduit et de nanoparticules d'or (rGO-AuNPs) via une réduction radiolytique induite par rayons gamma. La spectroscopie d'absorption UV-Vis, la spectroscopie infrarouge à transformée de Fourier, la spectroscopie Raman et la spectroscopie de photoémission des rayons X ont été utilisées pour évaluer de manière exhaustive le degré de réduction de l'oxyde de graphène et la formation des nanoparticules d'or. La microscopie à force atomique et la microscopie électronique à balayage ont été employées pour obtenir des informations morphologiques et topographiques sur les nanocomposites synthétisés. Les propriétés thermiques ont été étudiées par analyse thermogravimétrique et les propriétés électriques ont été investiguées à l'aide de la voltampérométrie cyclique et de la méthode de charge et décharge potentiostatiques. Les résultats ont démontré la réduction réussie de l'oxyde de graphène et des ions d'or par la transformation drastique des groupes fonctionnels contenant de l'oxygène et la formation de nanoparticules d'or. Les résultats de la caractérisation électrique ont mis en évidence d'excellentes propriétés électriques et un grand potentiel d’application dans le domaine des supercapacités.

Acknowledgment

First and foremost, I would like to express my deepest gratitude to my supervisor, Prof. Samy Remita, for his expertise in radiation chemistry and his unwavering guidance, assistance, and kindness throughout my internship. His support was indispensable for the completion of my internship.

I am also deeply thankful to Alexia Bistintzanos, Cyrille Sollogoub, Diana Dragoe, Florian Guinandie, Francois Muller, Matthieu Gervais, Michel Goldmann and Rasta Ghasemi for their collaboration and for allowing me to use various characterization instruments. Their help enabled me to obtain comprehensive results for my thesis, providing me with invaluable hands-on experience and a deeper theoretical understanding of many different instruments. Special thanks to Alexandre Demarque for gamma-ray training and reservation, Mireille Benoit for purchasing necessary reagents and instruments, Pascal Pernot for teaching me spectra deconvolution, and Zhenpeng Cui for additional supervision. I'm also grateful to all the professors, researchers, technicians, master and PhD students in ICP for creating a wonderful working atmosphere.

Moreover, I am tremendously appreciative of the European Commission's fully-funded financial support during my two years of master's study in Europe. I am also thankful to the EMJMD and SERP+ programs, as well as University of Paris-Saclay, University of Porto, University of Genova, and all the professors, classmates, and colleagues I met. These two years have been unforgettable, filled with numerous wonderful experiences.

Lastly, I want to thank my families, Tian Huang and other friends, and everyone who loves and supports me. I am deeply grateful to all of you who have been a part of this journey and to those reading my thesis now.

List of Abbreviations

AFM	Atomic Force Microscopy
AgNPs	Silver Nanoparticles
AuNPs	Gold Nanoparticles
CV	Cyclic Voltammetry
DMF	N,N-Dimethylformamide
EDLCs	Electric Double Layer Capacitors
EDX	Energy-dispersive X-ray Spectroscopy
FTIR	Fourier Transform Infrared
G	Pristine Graphene
GC	Glassy Carbon
GO	Graphene Oxide
IPA	Isopropanol
LMCT	Ligand-to-Metal Charge Transfer
LSPR	Localized Surface Plasmon Resonance
NPs	Nanoparticles
OFGs	Oxygen-containing Functional Groups
PCD	Potentiostatic Charge and Discharge
PET	Polyethylene Terephthalate
rGO	Reduced Graphene Oxide
SEM	Scanning Electron Microscopy
SERS	Surface Enhanced Raman Spectroscopy
TGA	Thermogravimetric Analysis
UV	Ultraviolet
Vis	Visible
V_{RHE}	Volts versus Reverse Hydrogen Electrode
V_{SHE}	Volts versus Standard Hydrogen Electrode
XPS	X-ray Photoemission Spectrometer

1. Introduction

Pristine graphene (G), as a classic one-atom-thick crystal, has been considered as a revolutionary material in the 21th century due to its exceptional mechanical, thermal, electronic and optical properties[1, 2] (charge-carrier mobility = 250 000 $cm^2 \cdot V^{-1} \cdot s^{-1}$ at room temperature,[3] thermal conductivity = 5000 $W \cdot m^{-1} \cdot K^{-1}$,[4] and mechanical stiffness = 1 TPa[5]). Nevertheless, common methods for graphene production, such as mechanical exfoliation from graphite[6, 7], epitaxial growth of graphene films[8, 9], and chemical vapor deposition[10-12], pose challenges for cheap and high-quality graphene production at an industrial scale. These methods are laborious, expensive, limited to small-scale production, and not yet fully developed[13, 14]. At present, a primary alternative strategy for large-scale graphene-like materials production involves oxidizing and exfoliating graphene into graphene oxide (GO) sheets, which are then reduced to obtain reduced graphene oxide (rGO), as illustrated in **Figure 1**. Despite being additionally decorated with structural defects and populated with oxygen-containing functional groups (OFGs) such as epoxy and hydroxyl groups mainly at the basal plane, and carbonyl and carboxyl groups mainly at the edge[13, 14], rGO possesses properties similar to pristine graphene due to its graphene-like structure. Moreover, this large-scale production method significantly reduces the costs, making the study of rGO increasingly appealing.

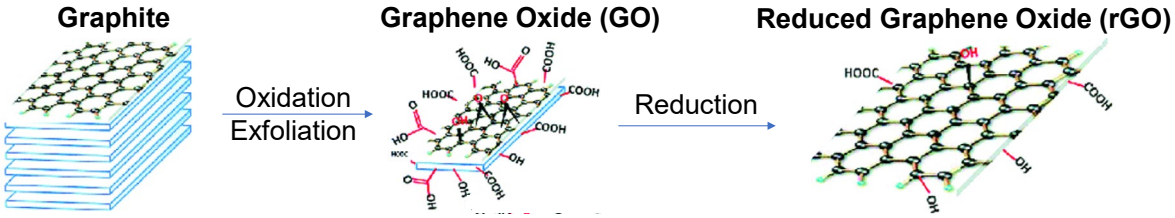

Figure 1 Schematic representation of the rGO production procedure

Currently, various methods for reducing GO into rGO have been developed, including chemical[15, 16], thermal[17, 18], electrochemical[19], microwave[20] and photo-assisted[21] thermal reduction methods. Nevertheless, each method has its own disadvantages and limitations. For instance, in chemical reduction, the introduction of reducing agents leads to difficulties in eliminating residual reducing agents and results in unpredictable properties deviating from those of pristine graphene[22]. Thermal reduction at high temperature inevitably damages the structure of rGO, along with a substantial quantity of weight loss (*ca.*30%)[23]. Electrochemical reduction can't be used for the large-scale production[24] while microwave- and photo-assisted methods are mainly employed to assist thermal reduction[25, 26]. Radiolytic reduction of GO has recently emerged and gradually been investigated since it overcomes most limitations of other reduction methods due to its advantages such as homogeneous reduction, affordability, no addition of reducing agents[27] and capability of large-scale production. Radiation sources can be classified into non-ionizing ones like UV light[28] and infrared photothermal reduction[29], and ionizing ones like electron beams[30], X-rays and Gamma (γ)-rays[31]. The key feature that differentiates non-ionizing and ionizing irradiation is whether the energy and ability of the radiation is capable of ionizing atoms and molecules. **Figure 2** presents a detailed

classification of the two main types of radiation.

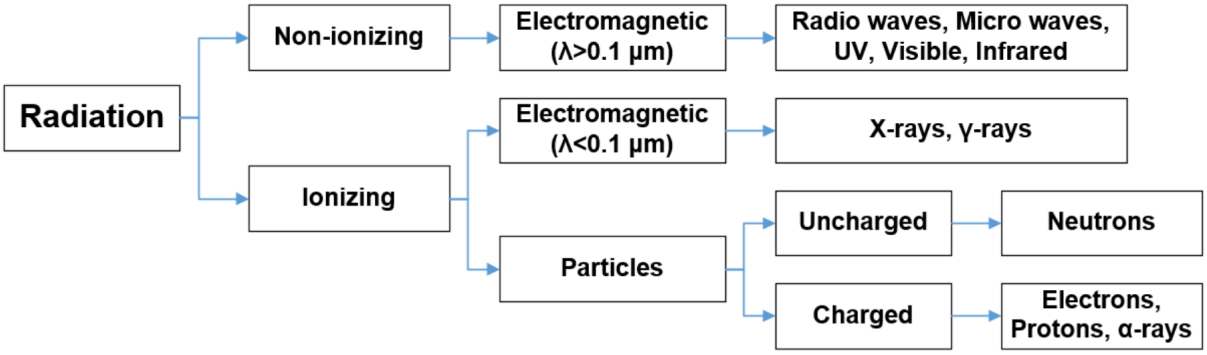

Figure 2 Classification of radiation types

Among various radiation types, γ-ray irradiation, a high-frequency electromagnetic radiation stemming from nuclear decay, has gradually been investigated due to its non-physical contact operation and precision[32]. The principle of gamma-irradiation for dilute aqueous solutions, also known as water radiolysis[33, 34], is that under gamma rays, reducing agents like solvated electrons (e_{aq}^-) and isopropanol radicals are generated from water at neutral pH by excitation or ionization under nitrogen atmosphere and in the presence of isopropanol ($(CH_3)_2CHOH$)[35]. Reduction is then achieved by solutes reaction with reducing agents, produced according to **Figure 3**.

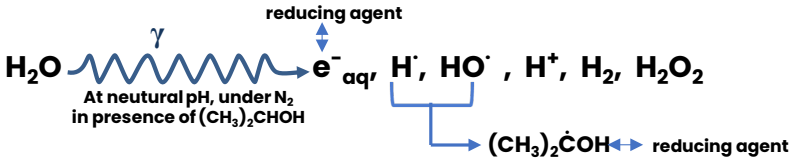

Figure 3 Schematic of gamma-induced water radiolysis

Previous recent works[27] in Institut de Chimie Physique (ICP) have demonstrated the feasibility of using γ-ray irradiation to reduce GO through water radiolysis. The obtained rGO exhibited a relatively high specific capacitance and an exponential capacitance-dose correlation, as depicted in **Figure 4a**. Additionally, single-layer graphene has a surface area close to 2600 $m^2 \cdot g^{-1}$ [36], making graphene-like materials such as rGO excellent platforms for the *in situ* growth of various species, like metal nanoparticles (NPs)[37, 38], for synthesizing rGO composites with synergistic properties[39]. On one hand, the abundant OFGs of precursor GO serve as reactive sites for the spontaneous reduction of metal ions, promoting the nucleation and growth of NPs on GO[40]. On the other hand, growing the NPs directly on GO sheets help prevent their agglomeration and overgrowth[41]. It has been demonstrated in the literature[42] that once functional materials are grown or anchored on rGO, the composites exhibit enhanced electron transport rates and high electrolyte contact area, leading to enhanced electrical properties, as shown in **Figure 4b**, which demonstrated the significantly increased specific capacitance of the obtained composites once silver nanoparticles (AgNPs) are anchored on rGO.

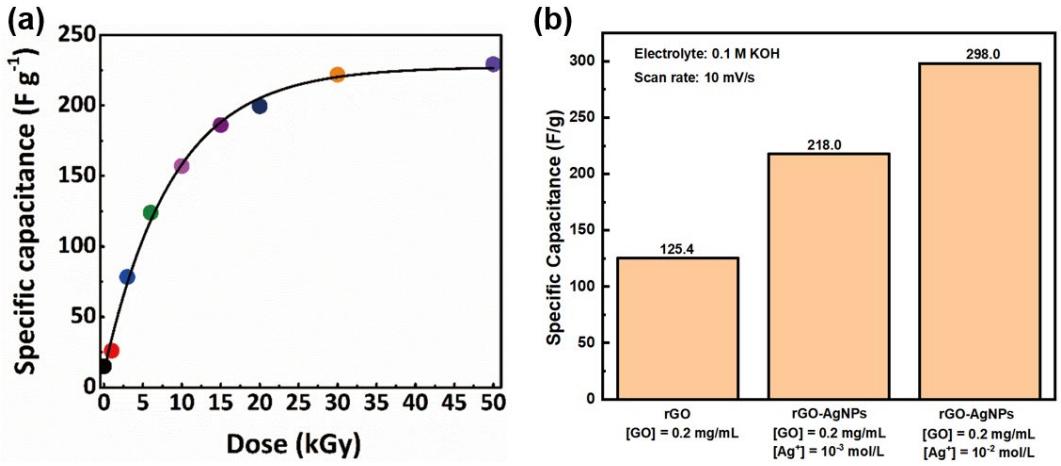

Figure 4 (a): Capacitance-dose correlation for GO under γ-ray irradiation[27] **(b):** Comparison of capacitance between radiolytic synthesized rGO and rGO-AgNPs composites[43]

The principle of radiolytic synthesis of metal NPs is also based on water radiolysis, where the generated reducing agents react with metal ions to form NPs. Similarly, as noble metal NPs, gold nanoparticles (AuNPs) are also expected to exhibit enhanced electrical properties when growing and anchoring on rGO sheets like silver. To verify this assumption, the objective of this internship is to synthesize rGO-AuNPs composites by simultaneous radiolytic reduction of GO into rGO and gold ions into AuNPs, as depicted by **Figure 5**. Multiple characterizations were conducted to provide a comprehensive evaluation of the reduction process, as well as exploration of the synthesized materials in the field of energy storage.

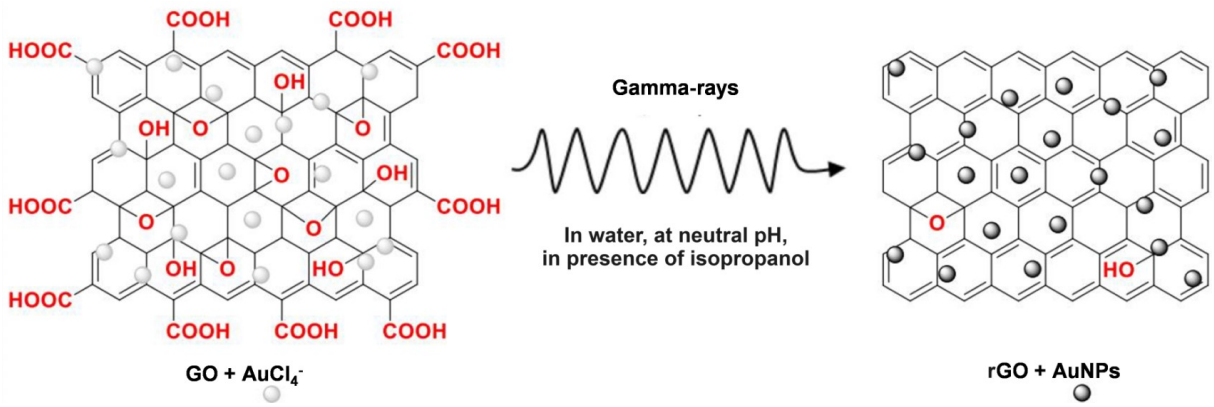

Figure 5 Global routine for the radiation-induced synthesis of rGO-AuNPs composites

2. Materials and Methods

2.1 Materials

Graphene Oxide (4 mg/mL, dispersion in H_2O), Potassium gold (III) chloride ($KAuCl_4$, 98%), and 2-Propanol (IPA, 99.9%) were purchased from Sigma-Aldrich and used as precursors. Distilled water (Millipore system 18.2 MΩ·cm^{-1}) was used as the solvent for radiolysis and as the reference for UV-Vis absorption spectra measurement. Nitrogen (N_2) gas

with 99.99% purity was purchased from Air Liquid Co for degassing. N,N-Dimethylformamide (DMF, 99.9%) purchased from Sigma-Aldrich was used to redissolve the synthesized nanocomposites for electrical experiments. In cyclic voltammetry (CV) measurements, Nafion perfluorinated resin solution (5 wt.% in a mixture of lower aliphatic alcohols and water, containing 45% water) was used as a binder. Potassium hydroxide purchased from Sigma-Aldrich was used as the electrolyte, and OP-U colloidal silica suspension purchased from Struers was used for electrode polishing. In supercapacitance fabrication, LOCTITE MR 3863 was used for depositing silver lacquer, and ionic liquid 1-Methyl-3-octylimidazoliumtriflate (99%) purchased from IOLITEC was used as the electrolyte. All chemicals were utilized as received without further purification.

2.2 Sample preparation

Aqueous solutions containing 0.2 $mg \cdot mL^{-1}$ GO (the molar mass of which is unknown), 0.2 $mol \cdot L^{-1}$ IPA, and $[AuCl_4]^-$ at two different concentrations (1×10^{-3} $mol \cdot L^{-1}$ and 5×10^{-4} $mol \cdot L^{-1}$) were prepared in 100 mL volumetric flasks for two different series. The volumetric flasks were thoroughly shaken to ensure complete dissolution. The solutions were then transferred into transparent glass vials (40 mL, 3 cm × 8 cm), and degassed with N_2 gas for 20 minutes to remove dissolved oxygen, which could inhibit the reduction process. Both the volumetric flasks and glass vials were covered with thin aluminum films to protect them from sunlight, as gold ions would be reduced and form AuNPs when exposed to sunlight.

2.3 Water irradiation and sample reduction

The process of water radiolysis, which has been summarized in **Figure 3**, can be further explained by the following equations. Firstly, at neutral pH and in the absence of oxygen, the radiolysis of water yields various reactive oxidizing and reducing species, including solvated electrons (e_{aq}^-), hydroxyl radicals ($HO^\bullet$), hydrogen atoms ($H^\bullet$), hydronium ions (H_3O^+), hydrogen peroxide (H_2O_2), and hydrogen molecule (H_2), as shown in **Equation 1**[44].

$$H_2O \xrightarrow{\gamma-rays} e_{aq}^-, HO^\bullet, H^\bullet, H_3O^+, H_2O_2, H_2 \qquad \textbf{Eq. 1}$$

The radiolytic yields (quantifying the amounts of molecules or free radicals generated per 1 Joule of deposited energy) of various species have been well established from previous study about water radiolysis[45], as shown in **Table 1**. Among the radical products, e_{aq}^- and $H^\bullet$ are reducing species with standard redox potential $E^\circ(H_2O/e_{aq}^-) = -2.9\ V_{SHE}$ and $E^\circ(H^+/H^\bullet) = -2.3\ V_{SHE}$, respectively, while $HO^\bullet$ radicals are strong oxidants with standard redox potential $E^\circ(HO^\bullet/H_2O) = +2.7\ V_{SHE}$[44, 46, 47].

Table 1 Radiolytic yields of the primary species from pure water by ^{60}Co rays

Radical Products ($mol \cdot J^{-1}$)	Molecular Products ($mol \cdot J^{-1}$)
$G(HO^\bullet) = 2.8\times10^{-7}$	$G(H_3O^+) = 2.8\times10^{-7}$
$G(e_{aq}^-) = 2.8\times10^{-7}$	$G(H_2O_2) = 0.7\times10^{-7}$
$G(H^\bullet) = 0.6\times10^{-7}$	$G(H_2) = 0.4\times10^{-7}$

To ensure reduction and $HO^\bullet$ consumption, IPA was introduced to convert $HO^\bullet$ into isopropanol radical ($(CH_3)_2\dot{C}OH$), which is also a strong reducing agent with a standard

redox potential $E^{\circ}\left((CH_3)_2CHOH/(CH_3)_2\dot{C}OH\right) = -1.8\ V_{SHE}$ at neutral pH[48, 49]. Simultaneously, $H^{\bullet}$ will also be converted into $(CH_3)_2\dot{C}OH$, through the following **Equations 2 and 3**.

$$(CH_3)_2CHOH + HO^{\bullet} \rightarrow (CH_3)_2\dot{C}OH + H_2O \quad \textbf{Eq. 2}$$

$$(CH_3)_2CHOH + H^{\bullet} \rightarrow (CH_3)_2\dot{C}OH + H_2 \quad \textbf{Eq. 3}$$

Therefore, the radiolytic yields of the two produced reducing agents are $G(e_{aq}^-) = 2.8\times10^{-7}$ mol·J^{-1}, $G((CH_3)_2\dot{C}OH) = G(H^{\bullet}) + G(HO^{\bullet}) = 3.4\times10^{-7}$ mol·J^{-1}, respectively. As a result, the concentration of each reducing agent is calculable, based on **Equation 4**:

$$c = D \times G \times d \quad \textbf{Eq. 4}$$

where c is the concentration of the generated reducing agents (mol·L^{-1}) D: the radiation dose in Grays (the amount of energy deposited in the irradiated media, 1 Gy = 1 J·kg^{-1}) and d: the density of the irradiated medium (kg·L^{-1}).

Both GO and gold ions can be reduced by reacting with these reducing agents. Despite the equation for GO reduction cannot be straightforwardly written, the reduction of gold ions to zero-valent metal NPs proceeds according to the following global equations[50]:

$$Au^{3+} + 3e_{aq}^- \rightarrow Au^0 \quad \textbf{Eq. 5}$$

$$Au^{3+} + 3(CH_3)_2\dot{C}OH \rightarrow Au^0 + 3CH_3COCH_3 + 3H^+ \quad \textbf{Eq. 6}$$

The zero-valent gold atoms (Au^0) then act as nucleation centers, facilitating further coalescence. Nucleation and coalescence are favored because all the NPs, possessing intense surface energy, are thermodynamically unstable or metastable. Additionally, the metal atom-atom binding energy is stronger than the atom-solvent or atom-ligand binding energies[51], promoting the formation of stable NPs.

$$Au^0 + Au^0 \rightarrow Au_2 \quad \textbf{Eq. 7}$$

$$Au_x + Au_y \rightarrow Au_{x+y} \quad \textbf{Eq. 8}$$

In this study, the ^{60}Cobalt in ICP was used as irradiation source, with a maximal dose rate at *ca.* 2.0 kGy/h, as shown in **Figure 6**. All the works were done under this maximal dose rate. Then the irradiation dose of each sample can be determined by controlling the irradiation time, based on **Equation 9**.

$$D\ (kGy) = \dot{D}(kGy/h) \times t\ (h) \quad \textbf{Eq. 9}$$

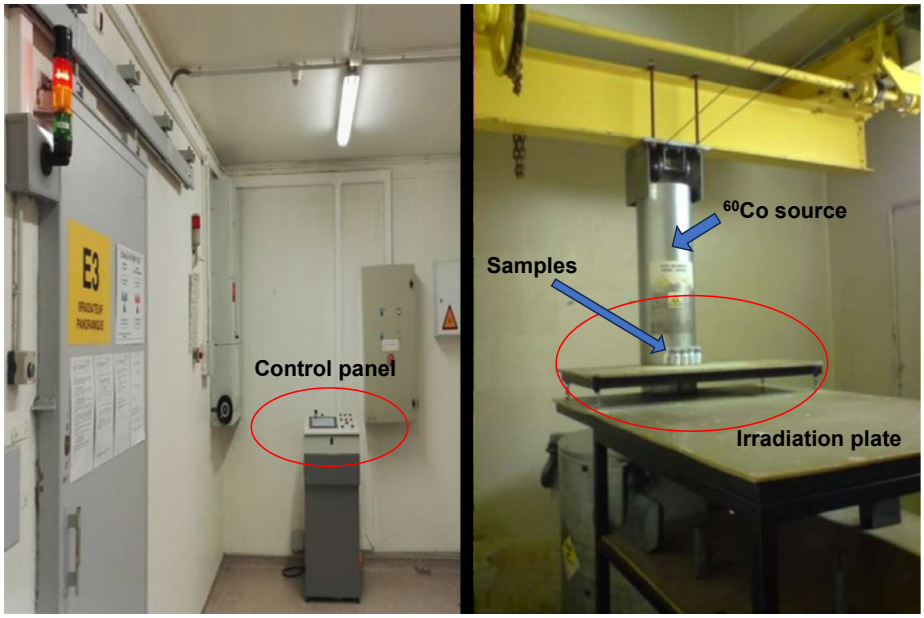

Figure 6 Phtotgraph of ^{60}Co gamma source

2.4 Characterizations

UV-Vis absorption spectroscopy was utilized to follow the evolution of GO and gold ions concentrations in sample solutions subjected to different irradiation doses. A Hewlett-Packard 8543 spectrophotometer with 2 mm thick quartz cuvettes was used in ICP. The UV-Vis absorption spectra were recorded in the optical range of 200-800 nm using distilled water as reference. All samples were measured immediately after gamma-irradiation, with a dilution factor of 3. The UV-Vis absorption spectra deconvolution was conducted using Docker and Spectra-kinetics analysis code developed by Prof. Pascal Pernot[52].

Fourier Transform Infrared (FTIR) spectroscopy was employed to detect the presence and intensity of various OFGs in the obtained nanocomposites. The analysis was conducted using a PerkinElmer Spectrum Two FT-IR Spectrometer in Conservatoire National des Arts et Métiers (le CNAM). The system was equipped with a KBr window and a $LiTaO_3$ detector. The scan range was extended from 4000 cm^{-1} to 700 cm^{-1} with a spectral resolution of 2 cm^{-1}. Solid samples were prepared by centrifugation of aqueous, irradiated samples at 7000 rpm for 10 minutes, then the sediments were dried at 100 °C for 24 h.

To investigate the degree of structural disorder in the obtained nanocomposites, Raman spectra were measured using an iHR550 imaging spectrometer in Institut des NanoSciences de Paris (INSP), Sorbonne University. A 532 nm incident laser was used and the Raman shift was selected from 1000 cm^{-1} to 3000 cm^{-1} with a spectral resolution of 2 cm^{-1}. 200 µL of each sample was drop-casted on a glass substrate and allowed to air dry for 24 hours.

For further surface elemental analysis, X-ray Photoemission Spectroscopy (XPS) was performed using a Thermo Fisher Scientific K-Alpha Spectrometer in Institut de Chimie Moléculaire et des Matériaux d'Orsay (ICMMO), University Paris-Saclay. An aluminum anode served as the monochromatic source (Al Kα = 1486.7 eV), and the X-ray angle was set

as 56°. The original data were processed using Avantage software. The same samples analyzed by ATR-FTIR were used for the XPS analysis.

Scanning Electron Microscopy (SEM) and Energy-Dispersive X-ray Spectroscopy (EDX) characterizations were conducted in École Normale Supérieure (ENS) Paris-Saclay, for morphological and elemental studies. A Hitachi S-3400n reference microscopy equipped with an X-ray detector was used. The accelerating voltage was adjusted between 5-10 kV, and the probe current was set in the range of 40-60 μA to optimize images quality. The same samples used for XPS characterization were attached to conductive carbon adhesive tab substrates.

In addition to SEM, Atomic force microscopy (AFM) was employed to obtain more detailed morphological information. The AFM analysis was performed using a Park NX20 Atomic Force Microscope in Institut des NanoSciences de Paris (INSP) with a silicon tip operating in tapping mode. Gwyddion Software was utilized for image processing. 200 μL of each sample was drop-casted on a SiO_2 substrate and allowed to air dry for 24 hours.

For thermal properties studies, Thermogravimetric Analysis (TGA) was conducted in Laboratoire Procédés et Ingénierie en Mécanique et Matériaux (PIMM), CNAM, using a TGA Q500 (TA instruments, USA) under an oxygen flow rate of 60 $mL \cdot min^{-1}$. The same solid samples after FTIR, XPS and SEM characterizations were analyzed. Between 1 to 5 mg of each sample was placed in an alumina crucible, and the heating rate was set at 10 $°C \cdot min^{-1}$.

Cyclic Voltammetry (CV) experiments were conducted in SATIE lab in CNAM using a CHI1222C Electrochemical Analyzer potentiostat and a conventional three-electrode cell setup. An Ag/AgCl (saturated KCl) electrode served as reference electrode, a platinum wire was used as counter electrode, and a glassy carbon (GC) electrode acted as working electrode, with 1 M KOH as the electrolyte. Samples before and after irradiation were dried and dissolved in DMF at a concentration of 0.2 g/L. Then, 180 μL of sample solution was mixed with 20 μL Nafion, which served as a binder. Subsequently, 10 μL of the sample was drop-casted on the working electrode and air-dried for 1 hour. Before each drop-cast, the GC electrode was polished by colloidal silica suspension and rinsed with ultrapure water. The voltage varied from -1.8 to 0.8 V, and scan rate varied from 10 to 100 $mV \cdot s^{-1}$.

Potentiostatic Charge and Discharge (PCD) experiments were carried out in Ecole d'ingénieurs - Campus de Paris (ECE) using a 5V constant voltage source and a SDS 1120CML+ Digital Storage Oscilloscope. The prepared solid samples were fabricated as a simple supercapacitor based on an approach from the literature. After centrifugation and drying, solid samples were redissolved into DMF at a concentration of 0.2 g/L. Then, 100 μL of the solution was drop-casted on glass substrate as electrode, ionic liquid 1-Methyl-3-octylimidazoliumtriflate as electrolyte to fabricate supercapacitor, the detailed process was described in chapter 3.7.

3. Results and Discussion

3.1 Visual characterization

Two series (A and B) were investigated, with the same concentration of GO (0.2 mg · mL^{-1}) and isopropanol (0.2 mol · L^{-1}) but different concentrations of $[AuCl_4]^-$. Each series was divided into 10 samples, each sample was subjected to irradiation for different durations, resulting in varying irradiation doses. The samples were labeled from 1 to 10, corresponding to increasing doses up to 55 kGy. Detailed concentrations and doses, as well as the photographs before and after irradiation are shown in **Figure 7**.

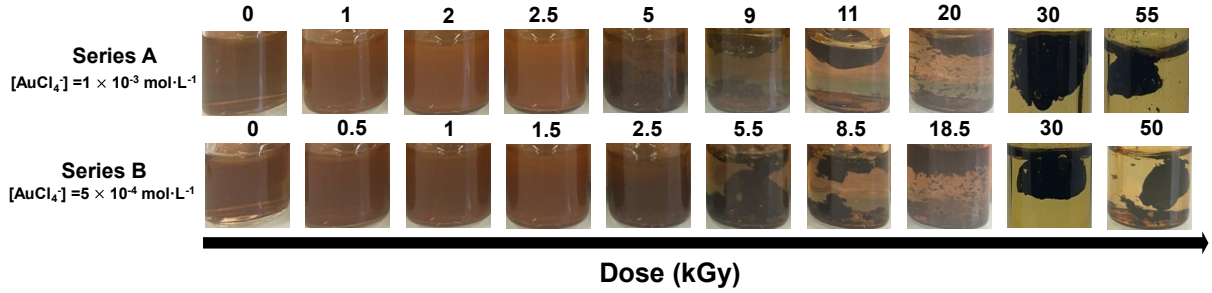

Figure 7 Photographs of sample solutions with increasing irradiation doses

As can be seen, with increase of the dose, the solutions in both series changed from clear to turbid, followed by a transition from homogeneous solutions to black powders suspensions, indicating that the amphiphilic GO was reduced to hydrophobic rGO, and eventually formed hydrogel-like structures, which suggests that due to the hydrophobic effect, the rGO started to aggregate, with some complex interactions with water during aggregation.

According to **Equation 4**, the theoretical doses which enable quantitively reduction of 10^{-3} mol·L^{-1} $[AuCl_4]^-$ can be calculated:

$$D = 3 \times \frac{c\ (mol \cdot L^{-1})}{G\ (mol \cdot J^{-1}) \times d(kg \cdot L^{-1})} = 3 \times \frac{10^{-3}}{(2.8 + 3.4) \times 10^{-7} \times 1} = 4.8\ kGy \sim 5\ kGy$$

In this equation, the factor 3 is used due to the valence of Au(III) which implies three steps of reduction by two reducing agents, IPA radicals and solvated electrons. Additionally, a slightly excessive dose is frequently used in practice to ensure the desired effect[43]. Therefore, the theoretical quantitative dose needed to reduce 10^{-3} mol·L^{-1} $[AuCl_4]^-$ (series A) could be approximately regarded as 5 kGy, and for 5×10^{-4} mol·L^{-1} $[AuCl_4]^-$ (series B), it is *ca.* 2.5 kGy. Previous work[43] has demonstrated that the theoretical quantitative dose to reduce 0.2 mg·mL^{-1} GO is 6 kGy. Thus, the theoretical quantitative doses which are required to quantitatively reduce GO and $[AuCl_4]^-$ in series A and B are 11 kGy and 8.5 kGy, respectively.

3.2 Kinetic studies by UV-Vis absorption spectroscopy and spectra deconvolution

The UV-Vis absorption spectra of the two series are shown in **Figure 8**. As can be seen, before irradiation, there are initially two intense bands: Band 1 at *ca.* 220 nm and Band 2 at *ca.*

300 nm. With increase of the irradiation doses, the decrease of the spectra intensity can be observed, demonstrating the gradual then complete reduction of both GO and $[AuCl_4]^-$. Besides, for Band 1, with increase of the doses, a red-shift from 220 nm to 265 nm was observed for both series.

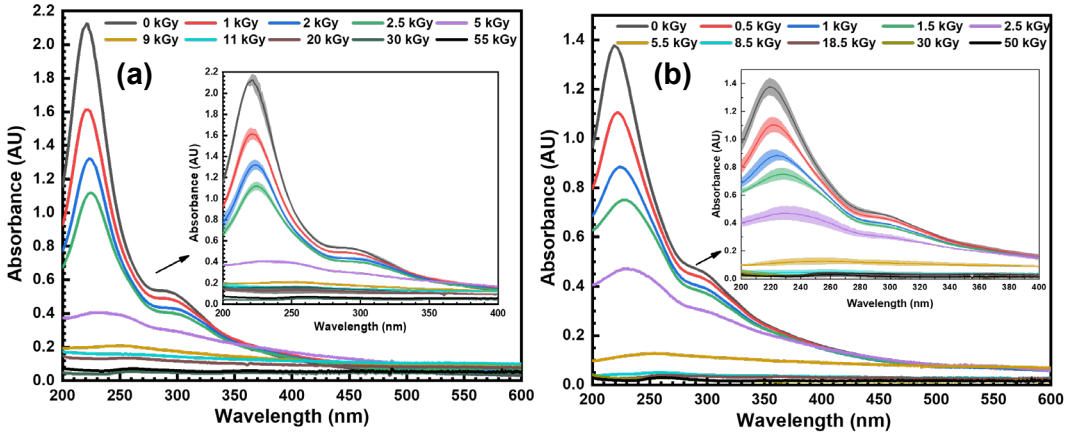

Figure 8 UV-Vis absorption spectra of the two series before and after irradiation (Dilution factor: 3, optical length: 2 mm) **(a)** series A (10^{-3} M) **(b)** series B (5×10^{-4} M)

To further study the UV-Vis absorption spectra, the extinction coefficient of GO and $[AuCl_4]^-$ in the wavelength range from 200 to 400 nm were measured by preparing gradient concentration solutions, as shown in **Figure 9**. It is worth noting that the exact molar mass of GO is unknown, leading to different units for the extinction coefficients of GO and $[AuCl_4]^-$. For GO, the band at *ca.* 230 nm is attributed to the $\pi \rightarrow \pi^*$ transition of the aromatic C=C bonds, indicative of the graphitic structure, while the band at *ca.* 295 nm corresponds to the $n \rightarrow \pi^*$ transition characteristic of carbonyl C=O groups[53, 54]. For $[AuCl_4]^-$, both bands represent electron transfer from ligand orbitals (specifically the 3p orbital of Cl) to holes in the 5d shell of Au (III), known as ligand-to-metal charge transfer (LMCT). The two LMCT bands at *ca.* 220 nm and 300 nm correspond to $p_\sigma \rightarrow d_{x^2-y^2}$ transition and $p_\pi \rightarrow d_{x^2-y^2}$ transition, respectively[55].

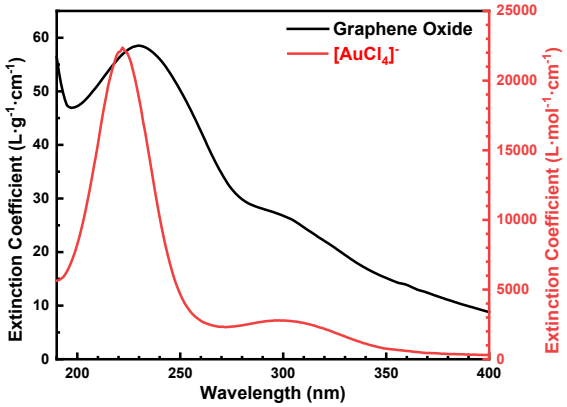

Figure 9 Extinction coefficients of GO and $[AuCl_4]^-$ in the wavelength range from 200 to 400 nm

Therefore, both of the two bands appearing in **Figure 8** are the results of overlapping. Band 1, at *ca.* 220 nm, is the GO band corresponding to the $\pi \rightarrow \pi^*$ transition of the aromatic C=C bond, overlapping with the LMCT band of $[AuCl_4]^-$. Band 2, at *ca.* 300 nm, is the GO band, corresponding to the $n \rightarrow \pi^*$ transition of the carbonyl C=O group, overlapping with the second LMCT band of $[AuCl_4]^-$. The observed red-shift of Band 1 from 220 nm to 265 nm suggests that, with the reduction of GO, there is a transition in carbon hybridization from an sp^3 hybridized state (attached to oxygen) to an sp^2 hybridized configuration, thereby regaining the π-conjugation within the GO structure, as mentioned in the literature[56]. This red-shift becomes apparent only when the dose reaches 9 kGy for series A and 5 kGy for series B, which exceed the theoretical quantitative dose for reducing $[AuCl_4]^-$. This suggests that for both series, the reduction of $[AuCl_4]^-$ is much faster than that of GO, reduction of GO is obvious only after when $[AuCl_4]^-$ is almost completely reduced.

It is worth noting that the Localized Surface Plasmon Resonance (LSPR) band of AuNPs at *ca.* 540 nm, observed in the absence of GO, cannot be found in **Figure 8**. Similarly, in other UV-Vis absorption spectroscopies studies of rGO-AuNPs, this LSPR band also disappears or significantly decreases in intensity. This phenomenon has often been attributed to the low concentration of gold ions or left unexplained[39, 57-59], which are not convincing enough. In fact, the LSPR of AuNPs is highly sensitive to their surroundings; when AuNPs are attached to rGO, the higher dielectric constant of rGO alters the local refractive index around the AuNPs, thereby affecting the resonance conditions and leading to modifications in the LSPR band intensity. Moreover, the charge and energy transfer between AuNPs and rGO which alter the electron density and plasmonic behavior of AuNPs, further decrease the LSPR band intensity[60, 61]. Therefore, the decrease or disappearance of LSPR band could be reasonably considered as evidence that the formed AuNPs are attached to rGO rather than suspended in solutions.

To further investigate the kinetics of radiation induced reduction, spectra deconvolutions, based on the literature[52, 62] were conducted for both series. The principle of deconvolution lies in utilizing the known extinction coefficients of both GO and $[AuCl_4]^-$ at each wavelength shown in **Figure 9** as limitations to calculate the remaining concentration of both GO and $[AuCl_4]^-$ under various irradiation time from the absorbance, based on the Beer Lambert's Law. One equation with two unknown concentrations can be formulated at each wavelength, and then these equations are combined to solve for the most accurate concentration of GO and $[AuCl_4]^-$. The deconvolution results are shown in **Figure 10**. From these results, it is evident that for both series, reduction of $[AuCl_4]^-$ is much faster than that of GO. For series A, as expected, 5 kGy is needed for the reduction of 10^{-3} M $[AuCl_4]^-$, while reduction of GO becomes significant at dose above 5 kGy and is completed at *ca.* 11 kGy. Similarly, for series B, 2.5 kGy is needed for the reduction of 5×10^{-4} M $[AuCl_4]^-$, with GO reduction becoming significant at dose above 2.5 kGy and completed at *ca.* 8.5 kGy. Once $[AuCl_4]^-$ is completely reduced, the reduction rate of GO significantly increases, indicating the potential electron transfer between $[AuCl_4]^-$ and GO. Nevertheless, our deconvolution method has limited accuracy. Firstly, it could not take the red-shift of Band 1 into consideration. Furthermore, as shown in **Equation 1**, the formation of H_3O^+ leads to the gradual pH decrease during

irradiation and it has been demonstrated that[63] the LMCT band of $[AuCl_4]^-$ at *ca.* 300 nm also experiences a red-shift and intensity increase when the pH decreases from neutral, which is also incapable of being taken into consideration by deconvolution. The accuracy of deconvolution is also constrained by the limited number of samples subjected to different irradiation doses. Despite these limitations, it still can be roughly concluded that for both series, $[AuCl_4]^-$ is predominately reduced initially, and GO is mainly reduced only after $[AuCl_4]^-$ is almost completely consumed.

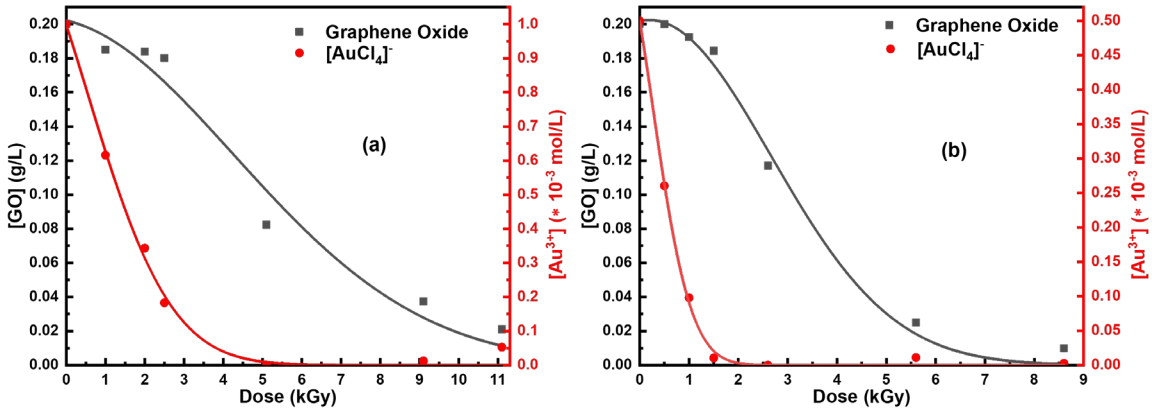

Figure 10 UV-Vis spectra deconvolution results. **(a)** series A (10^{-3} M) **(b)** series B (5×10^{-4} M)

3.3 Structural studies by FTIR and Raman spectroscopies

FTIR is sensitive to the various vibrational modes of different OFGs, making it a useful tool for evaluating the reduction degree of GO by measuring the intensity changes of OFG peaks during irradiation. As shown in **Figure 11**, the peaks at different wavenumbers represent various vibrational modes of OFGs. For both series before irradiation, the broad band ranging from *ca.* 3650 to 1800 cm^{-1} indicates the presence of hydroxyl and carboxylic groups (O-H stretching vibration), with a high degree of intermolecular hydrogen bond interaction. Additionally, peaks at *ca.* 1727 cm^{-1} (C=O stretching vibration), *ca.* 1364 cm^{-1} (O-H in-plane deformation vibration), *ca.* 1219 cm^{-1} and *ca.* 1065 cm^{-1} (C-O stretching vibration) highlight the presence of various OFGs on GO, such as epoxy, carboxylic and hydroxyl groups[64, 65]. The peak at *ca.* 1617 cm^{-1} (C=C stretching vibration) indicates that some conjugation remains in GO, despite the abundance of OFGs. The observed main peaks are consistent with FTIR spectra of GO reported in the literature[66]. With the increase in irradiation dose, the intensity of most peaks significantly decreases, demonstrating the successful elimination of OFGs through irradiation.

It is worth noting that the attached AuNPs cannot be detected by FTIR since FTIR spectroscopy primarily reveals the vibrational modes of chemical bonds, while the interaction between rGO and AuNPs are mainly non-covalent, such as van der Waals forces, π-π stacking, or electrostatic interactions. Metallic bonds in AuNPs do not exhibit the dipole moment changes necessary for IR absorption.

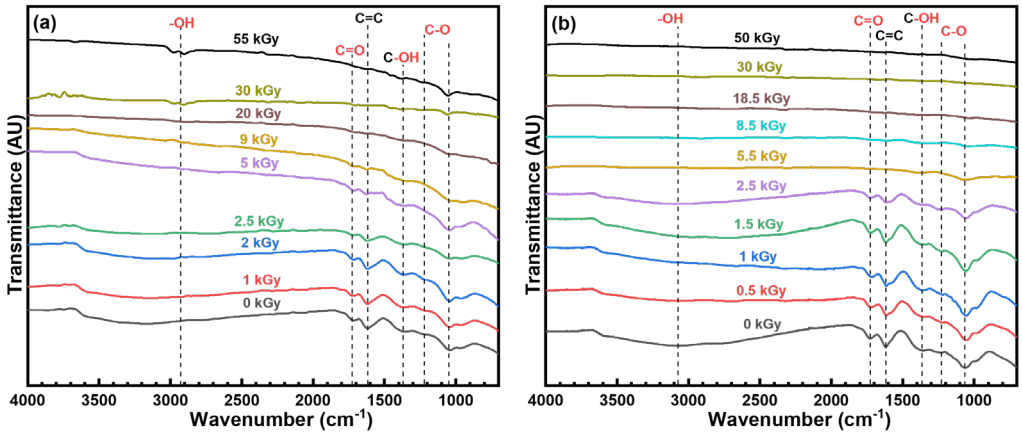

Figure 11 FTIR spectra of two series before and after irradiation.
(a) series A (10^{-3} M) **(b)** series B (5×10^{-4} M)

Raman spectroscopy has been frequently used for studying carbon-based materials, playing a crucial role in structural characteristics study by analyzing the main Raman bands. For GO-based materials, the D band, located at *ca.* 1350 cm^{-1}, originates from a second-order process and is associated with defects or disorder due to the presence of OFGs. The G band, at *ca.* 1582 cm^{-1}, arises from a normal first-order Raman scattering process in graphene, corresponding to the in-phase vibration of the graphite lattice (carbon sp^2)[67]. Additionally, there are also some second-order Raman bands, including overtones like the 2D band, and combinations such as the D+G band. As shown in **Figure 12a**, all the bands mentioned above were clearly observed in the Raman spectra of series A. Additionally, the increased intensity of the D band suggests that the reduction process introduced defects into the structure of GO[68].

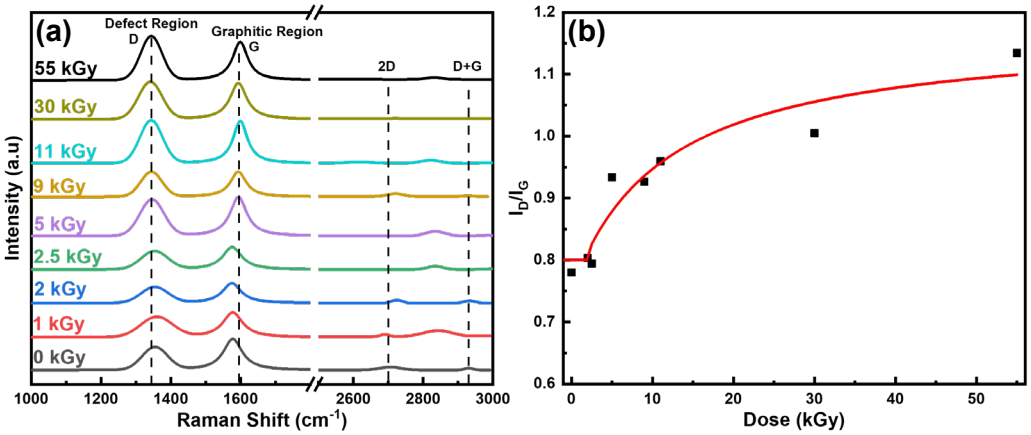

Figure 12 (a) Raman spectra of series A (10^{-3} M) before and after irradiation (b) Evolution of I_D/I_G ratio with irradiation

One of the most important parameters in Raman spectra is the intensity ratio between the D and G band (I_D/I_G), which reflects the degree of structural disorder[69]. The evolution of I_D/I_G

ratio with irradiation dose for series A are depicted in **Figure 12b**. As can be seen, this ratio remained constant at low doses, followed by an exponential increase at high doses, indicating again the reduction of $[AuCl_4]^-$ is much faster than GO, consistent with the results of kinetic studies. Depending on the reduction methods and the specific parameters used during Raman characterization, this ratio for GO and rGO ranges widely from 0.67 to 1.4 and 0.91 to 1.9[70-72], respectively. An increase in the I_D/I_G ratio indicates a decrease in the average size of sp^2 clusters[73], which is due to the formation of new, smaller sp^2 clusters during irradiation[74, 75]. Raman spectra of series B exhibit similar trend (not shown).

Similar with FTIR, Raman spectroscopy is also incapable of detecting AuNPs due to selection rules. However, the Raman signal can be significantly enhanced by conjugated rGO and especially by AuNPs. As shown in **Figure 12a**, the intensity of D and G bands increased at high doses. This special property has frequently been applied in Surface Enhanced Raman Spectroscopy (SERS).

3.4 Elemental studies by EDX and XPS

EDX and XPS were utilized for elemental analysis. The elemental distributions of series A, obtained by EDX before and after irradiation at the maximal irradiation doses (55 kGy), are shown in **Figure 13**. The homogeneous distribution of carbon (red color) and oxygen (bule color) remained consistent after irradiation. Initially, a tiny amount of gold (blue color) was detected due to gold salt precipitation as the solvent evaporated. After irradiation, the amount of gold significantly increased, demonstrating the formation of AuNPs. These AuNPs were attached to rGO and basically would not be separated by centrifugation. Similarly, series B also exhibited a consistent homogeneous distribution of carbon and oxygen after irradiation, along with an increased amount of gold. The EDX results of series B are also similar (not shown).

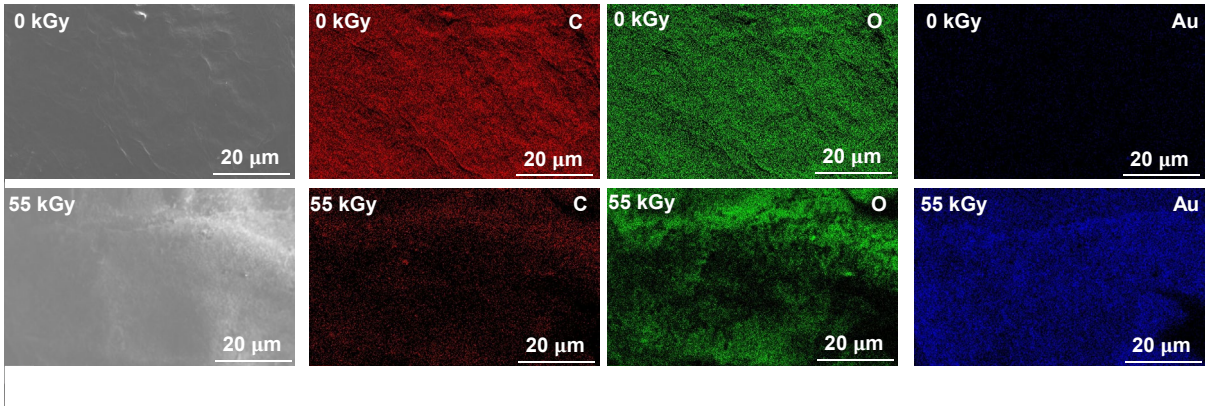

Figure 13 EDX maps of carbon, oxygen and gold distribution of series A (10^{-3} M) before and after irradiation

Figure 14 depicts the evolution of C/O ratio with irradiation dose for the two series, as obtained by EDX. Indeed, the C/O ratio is an important parameter for evaluating the reduction degree of GO. At lower doses, for both series, the C/O ratio remains constant, indicating that $[AuCl_4]^-$ was reduced firstly while GO almost remained unreduced. Subsequently, there is an

exponential increase in this ratio, demonstrating the consumption of OFGs. This ratio increased from 2.0 to 9.0 for series A (55 kGy) and 2.4 to 9.5 for series B (50 kGy), demonstrating the effective consumption of OFGs of our approach compared to other methods described in the literature. For reference, the C/O ratio for rGO typically falls in the range of 5.9 to 9.5, and 5.1 to 6.2 by chemical[15, 76-78] and thermal[16, 17, 79] reduction, respectively. The evolution of C/O ratio with irradiation is consistent with kinetic studies and Raman results.

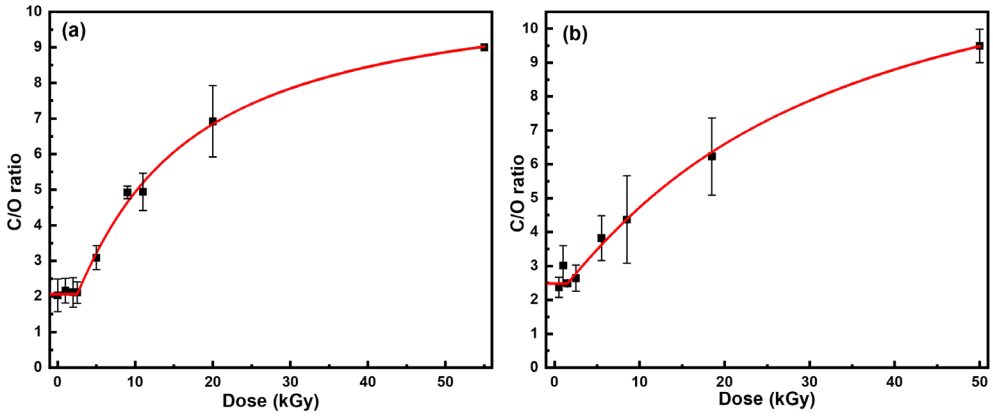

Figure 14 Evolution of C/O ratio of two series with irradiation.
(a) series A (10^{-3} M) **(b)** series B (5×10^{-4} M)

The formation of AuNPs and the recovery of conjugation are further demonstrated by XPS. For series A, initially, within the binding energy range from 200 to 800 eV, only C1s and O1s peaks were observed as depicted in **Figure 15a**, indicating the high purity of our rGO after irradiation, which is a key advantage of irradiation reduction compared to various chemical reduction methods[77, 78]. The intense O1s peak of GO before irradiation indicates the presence of abundant OFGs, while the gradual decrease in the intensity of this peak demonstrates the successful reduction of OFGs. The C/O ratio shown in **Figure 15b** further corroborates the reduction of OFGs. The exponential increase in the C/O ratio, reaching a final value of 7.4 at 55 kGy, is slightly lower than the value obtained by EDX (9.0) while the initial C/O ratio before irradiation and at lower doses are quite similar, both close to 2.0. This discrepancy arises because EDX probes a deeper region, typically down to a few micrometers, providing near-surface compositional information. In contrast, XPS is highly surface-sensitive, analyzing only the top few nanometers of the material. After reduction, rGO tends to restack, resulting the bulk being composed mainly of several layers of carbon skeleton basal plane sheets, where contain more carbon. Meanwhile, the remaining OFGs are primarily attached to the surface. Thus, theoretically, the bulk C/O ratio is higher than the surface C/O ratio, which aligns well with the experimentally results of EDX and XPS. Despite the discrepancy, the C/O ratio curves obtained by both EDX and XPS exhibit an exponential shape, demonstrating the effective reduction achieved by our radiolytic-induced approach. **Figure 15c** illustrates the C1s XPS spectra of series A before and after irradiation, revealing two discernible peaks: one attributed to sp^2 carbon at 284.4 eV and another to C-O at 286.4 eV. Normalization results, based on sp^2 carbon, exhibit a decrease in the intensity of C-O band, suggesting once again

the consumption of OFGs. **Figure 15d** presents the evolution of Au4f spectra of series A with irradiation dose. A splitting into two peaks at 84.2 eV and 87.9 eV, corresponding to $Au4f_{7/2}$ and $Au4f_{5/2}$, respectively, is observed due to spin-orbit coupling, consistent with the XPS spectra of Au4f reported in the literature[80]. The presence of gold peaks before irradiation is attributed to precipitated gold salt, while the significantly increased intensity during irradiation highlights the formation of AuNPs.

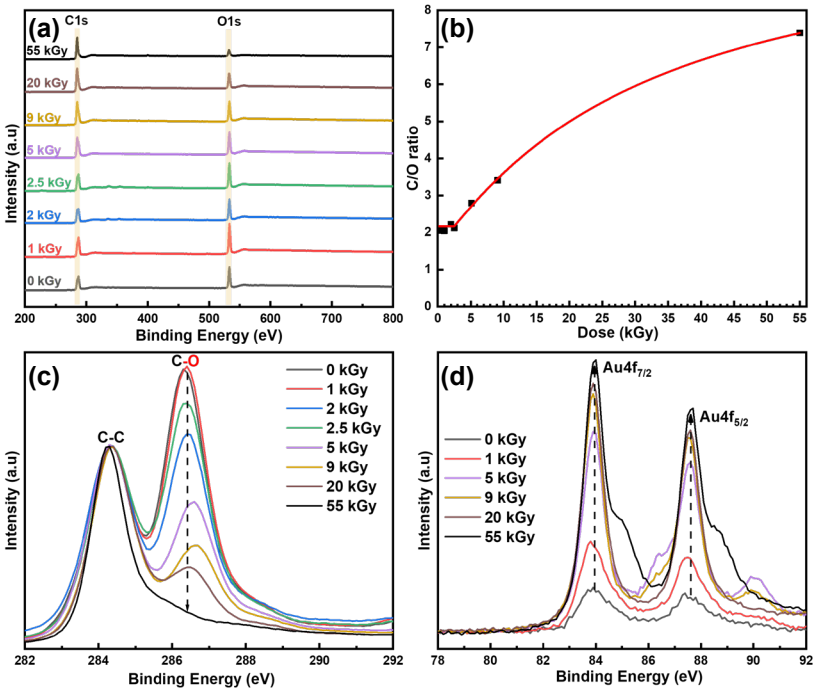

Figure 15 (a) XPS spectra of series A (10^{-3} M) as a function of irradiation dose (binding energy: 200 to 800 eV) **(b)** Evolution of C/O ratio with irradiation **(c)** High-resolution XPS C1s single spectrum **(d)** High-resolution XPS Au4f single spectrum

Figure 16 depicts the deconvolution results of XPS C1s spectra at various doses for series A. Peaks centered at 284.2, 284.9, 286.8, 288.5, and 291.2 eV correspond to carbon sp^2 (C=C), carbon sp^3 (C-C), hydroxyl and epoxy (C-O), carboxyl and carbonyl (C=O) groups, and the $\pi \rightarrow \pi^*$ shake up band[81, 82], respectively. The shape and intensity of all peaks remain almost identical at doses up to 2.5 kGy, indicating again that reduction of $[AuCl_4]^-$ is much faster than that of GO, which remains unreduced at lower doses. At a dose of 9 kGy, the intensity of sp^3 carbon peak and all the OFG peaks begin to decrease, while the intensity of sp^2 carbon peak increases. This demonstrates the effective reduction of GO and the recovery of conjugation. At maximal irradiation doses, the sp^2 carbon peak becomes the most intense, indicating a high degree of radiolytic reduction. XPS spectra and spectra deconvolution of series B exhibit similar trends (not shown).

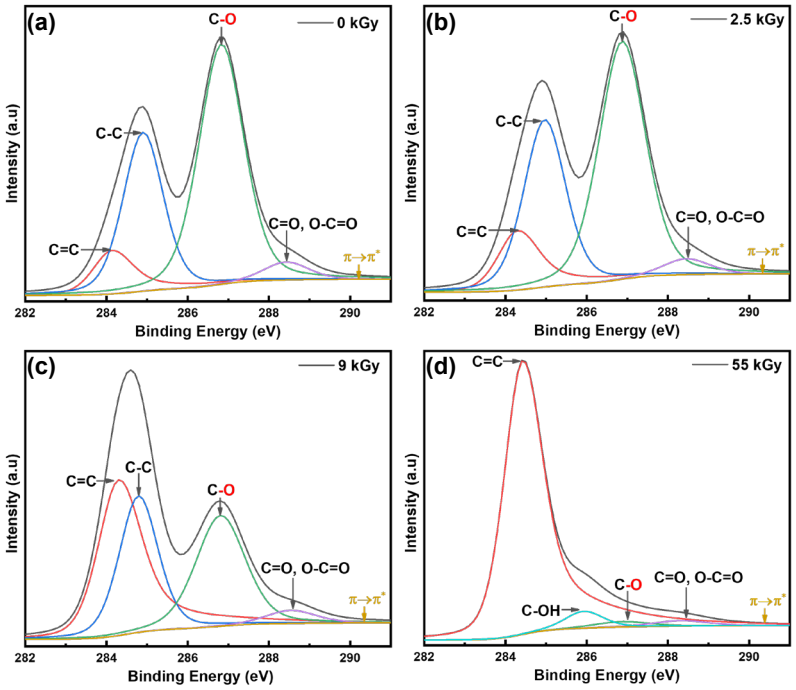

Figure 16 Evolution of deconvoluted XPS C1s spectra of series A (10^{-3} M) at different irradiation doses. **(a)** 0 kGy **(b)** 2.5 kGy **(c)** 9 kGy **(d)** 55 kGy

3.5 Morphological studies by SEM and AFM

Figure 17 depicts the morphology of series A (10^{-3} M) solid samples at different doses. Both rGO and AuNPs have excellent electrical conductivity, allowing clear images to be obtained without further sample treatment. Initially, before irradiation, flat and smooth GO layers were observed with a few amounts of precipitated gold salts attached. At a dose of 11 kGy, a significant morphological change of GO was clearly observed, transferring from smooth to quite rough. This change is attributed to the elimination of OFGs and the introduction of defects during irradiation. At maximal irradiation doses, the rGO become smooth again, possibility due to the extensive elimination of OFGs, which induces the aggregation of rGO. Additionally, a large amount of spherical AuNPs was clearly observed at lower scale. The amount of AuNPs significantly increased during irradiation, reaching a maximum at the highest doses. A polydisperse size distribution of gold particles, ranging from tens to hundreds of nanometers, was also clearly observed.

AFM was utilized for higher resolution morphological study and the representative images of the materials in case of series A are shown in Figure 18. Initially, before irradiation, single, double and triple GO layers were clearly observed, with lateral dimensions ranging from hundreds of nanometers to less than 10 micrometers. The thickness of each single GO layer is *ca*. 1 nm, highly consistent with values reported in the literature[83]. Notably, some wrinkles in the GO were also observed, which may affect the electrical properties due to the breakage of the conjugation[84]. At maximal irradiation dose, single layer rGO with a large amount of attached AuNPs was observed. The rGO appeared smoother, consistent with SEM

images; the thickness of rGO single layer remained *ca.* 1 nm and the size of the AuNPs ranged from several to tens of nanometers. Most AuNPs were anchored on rGO, while some were deposited directly on SiO_2 substrate. Two AuNPs with diameters of 12.3 nm and 13.8 nm were successfully observed and measured. It is noteworthy that due to the artefacts, the vertical height of the AuNP is more accurate and closer to the actual diameter of AuNP compared to the lateral distance. Combined images from SEM and AFM highlight a relatively polydisperse size distribution of AuNPs, ranging from several to hundreds of nanometers. The SEM and AFM images of series B exhibit similar phenomena (not shown).

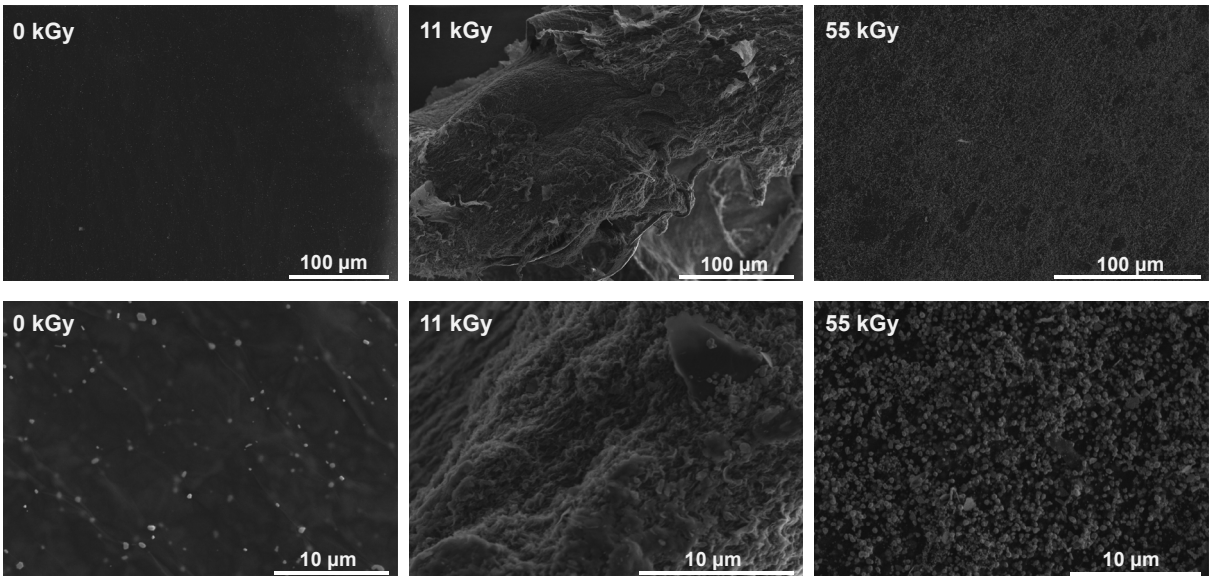

Figure 17 SEM images of series A (10^{-3} M) before and after irradiation at different scales.

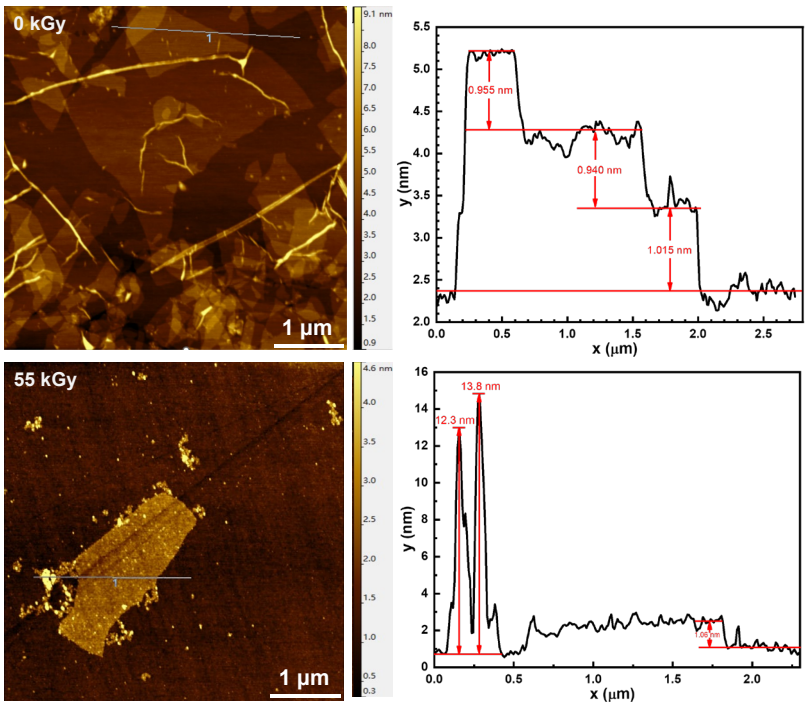

Figure 18 AFM images of series A (10^{-3} M) before and after irradiation and corresponding height profiles.

3.6 Thermal properties studies by TGA

Previous TGA studies of GO revealed two distinct stages of weight loss. The first stage with approximately 30% mass loss at *ca.* 200 °C, was attributed to the thermal decomposition of unstable OFGs. The second stage, with about 40% mass loss between 400-500 °C, was primarily attributed to the combustion of the carbon skeleton[85]. As depicted in **Figure 19**, the TGA results for both series before irradiation are in line with the literature. For both series after irradiation, there is a significantly decrease in mass loss in the first stage, indicating that most OFGs have been successfully reduced. This also results in enhanced onset temperatures for decomposition in the second stage, suggesting improved thermal stability due to a lower defect density in the rGO samples[86]. Furthermore, the high thermal stability of AuNPs, with a melting temperature of *ca.* 1064.3°C[87], ensures that there is no mass loss of AuNPs within the TGA temperature range. Consequently, the final weight percentage can be attributed to the mass fraction of AuNPs, which is 45.2% for series A and 34.7% for series B, after exposure to maximal irradiation dosess. These experimental results closely match the theoretical predictions of 49.6% for series A and 33.0% for series B, indicating both GO and gold ions in solution have been sufficiently reduced.

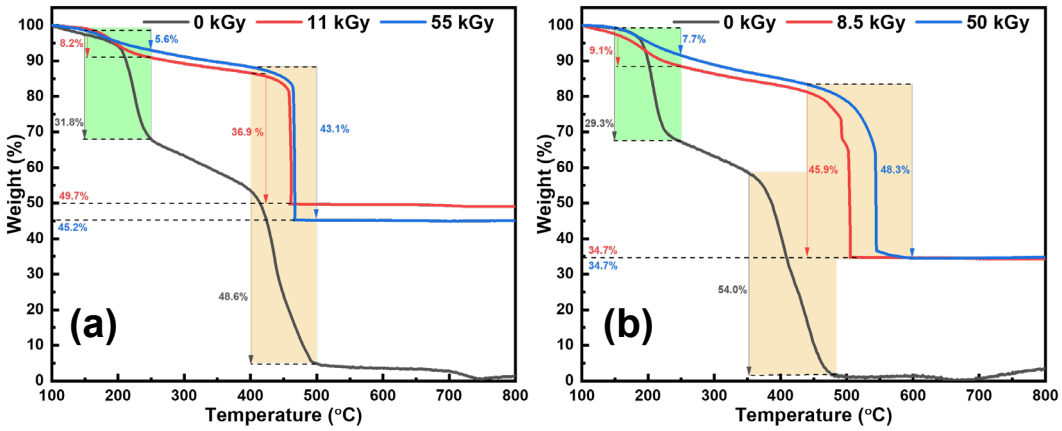

Figure 19 Thermogravimetric analysis of both series before and after irradiation.
(a) series A (10^{-3} M) **(b)** series B (5×10^{-4} M)

3.7 Electrochemical Analysis

Due to the recovery of conjugation and the formation of AuNPs, the radiolytically synthesized nanocomposites rGO-AuNPs are expected to exhibit enhanced electrochemical properties, making them highly promising for energy storage applications. CV and PCD experiments were conducted to quantitively study the electrochemical properties of the synthesized nanocomposites at different doses.

The cyclic voltammograms of series A, with scan rate ranging from 10 to 100 $mV\cdot s^{-1}$, are depicted in **Figure 20a-c**. The results illustrate a direct proportionality of the non-faradaic current to the scan rate, indicating capacitive behavior. The area of the CV curves increases after irradiation, demonstrating the enhanced specific capacitance by radiolytic reduction. Additionally, all CV curves exhibit a rectangular shaped hysteresis loop, characteristic of the

electric double layer capacitor (EDLCs), which indicates the diffusion mechanism of ions into the rGO-AuNPs composite electrodes[88].

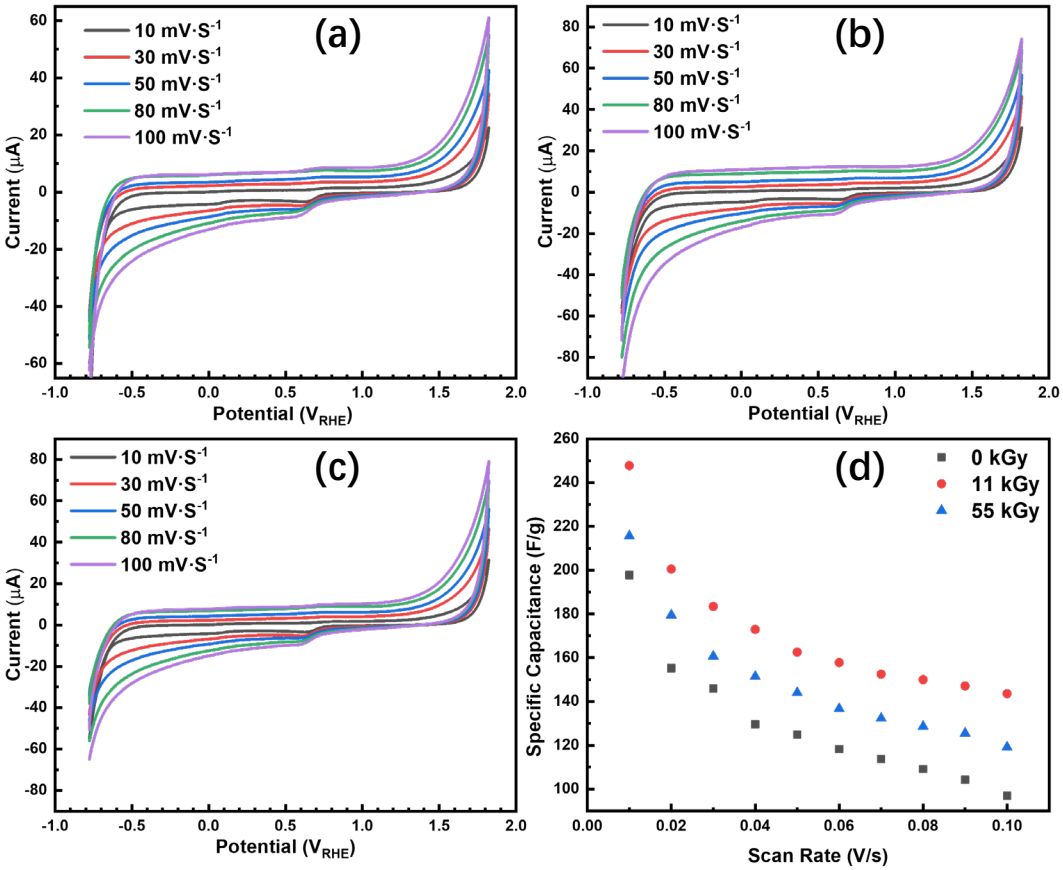

Figure 20 Cyclic voltammograms of series A (10^{-3} M) before and after irradiation **(a)** 0 kGy **(b)** 11 kGy **(c)** 55 kGy **(d)** Specific capacitance – scan rate correlation

The specific capacitance values can be calculated from the CV curves using the following **Equation 10**:

$$C = \frac{\int idV}{\Delta V \times m \times \nu} \qquad \textbf{Eq. 10}$$

where C represents the specific capacitance in $F \cdot g^{-1}$, $\int idV$ specifies the integral area of one complete CV curve, ΔV is the potential window (V), 'm' denotes the weight of the active material on working electrode (g) and 'ν' is the scan rate ($V \cdot s^{-1}$). The calculated specific capacitances of samples before and after irradiation at various scan rates are shown in **Figure 20d**. The specific capacitance is inversely proportional to the scan rate, since lower scan rates favor ion diffusion at the EDL, while higher scan rate results in lower ion migration, making charge storage less effective[89]. The composites irradiated at 11 kGy exhibit better specific capacitance compared to those at 55 kGy. This may be because excessive doses introduce too many defects, disrupting the structure of basal plane and thus decreasing capacitance.

Compared with other reduction methods, the specific capacitance of chemically reduced

rGO by hydrazine hydrate is 135 $F \cdot g^{-1}$ in 5.5 M KOH[90] and 49.9 $F \cdot g^{-1}$ in 1.5 M KOH[91]. The specific capacitance of electrochemically reduced rGO is 223.6 $F \cdot g^{-1}$ at 5 $mV \cdot s^{-1}$ in 1 M H_2SO_4[92], and thermally exfoliated rGO is 117 $F \cdot g^{-1}$ in H_2SO_4[93]. It is worth noting that due to the differences in morphology, the concentration and distribution of OFGs and defects, and various parameters in CV measurements, the obtained capacitance can vary significantly. Nevertheless, it can be concluded that radiolytically reduced rGO-AuNPs composites exhibit satisfactory capacitance, reaching 247.7 $F \cdot g^{-1}$ at 10 $mV \cdot s^{-1}$ in 1 M KOH at 11 kGy. Furthermore, compared to previous studies[27], the formation of AuNPs in the composites leads to an increase in capacitance. The CV curves of series B exhibit similar phenomena (not shown).

For PCD experiments, a new approach based on the literature[94] for supercapacitor fabrication was used, the process of which is schematically illustrated in **Figure 21**. Initially, the prepared solid samples, after centrifugation and drying, were redissolved into DMF at a concentration of 0.2 g/L. Then, 100 µL of the solution were drop-casted onto a glass substrate forming a graphene-comb pattern as two electrodes. Next, silver lacquer, a type of conductive lacquer, was deposited at both ends of the graphene combs and air dried for 24 hours to ensure the connection of the electrode and external electrical wires, forming a circuit. As an electrical insulation, a polyimide film called Kapton was used to isolate the silver points from the center area. Finally, 100 µL of the ionic liquid 1-Methyl-3-octylimidazoliumtriflate was drop-casted into the center area as the electrolyte. A polyethylene terephthalate (PET) sheet was covered on top of the ionic liquid to promote spreading, and Kapton was used again to ensure a seal without leakage. A real image of the fabricated supercapacitor is shown in **Figure 22a**.

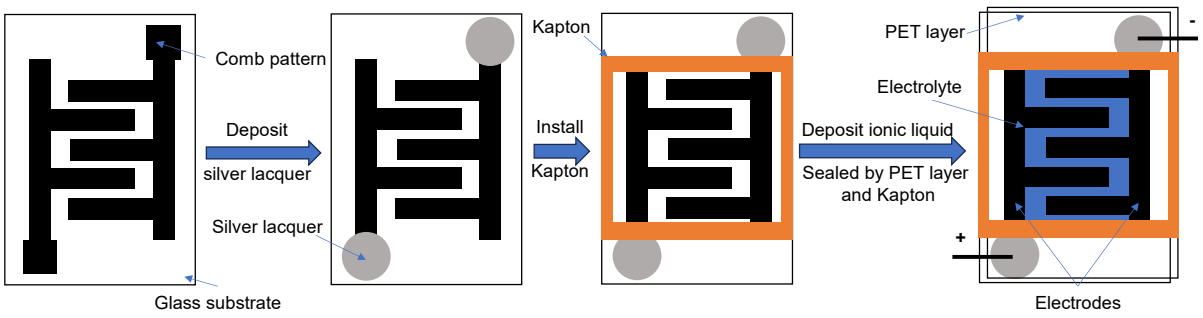

Figure 21 Schematic illustration of the rGO-AuNPs supercapacitor fabrication

PCD was then carried out by connecting the supercapacitor to a 5V constant voltage source and a resistor, controlling the switch to realize charging and discharging. One representative curve is shown in **Figure 22b** for series A. Based on the corresponding charge and discharge equations, the specific capacitances were calculated by exponential fit and the results are shown in **Figure 22c**. Due to the different electrolytes and approaches used, direct comparison with the specific capacitances obtained by CV is less meaningful; nevertheless, they are of same order of magnitude. The enhanced capacitance after irradiation can also be clearly visualized. The specific capacitances of series B obtained by PCD exhibit similar results (not shown). The electrochemical analysis demonstrated the excellent electrical properties of our synthesized composites.

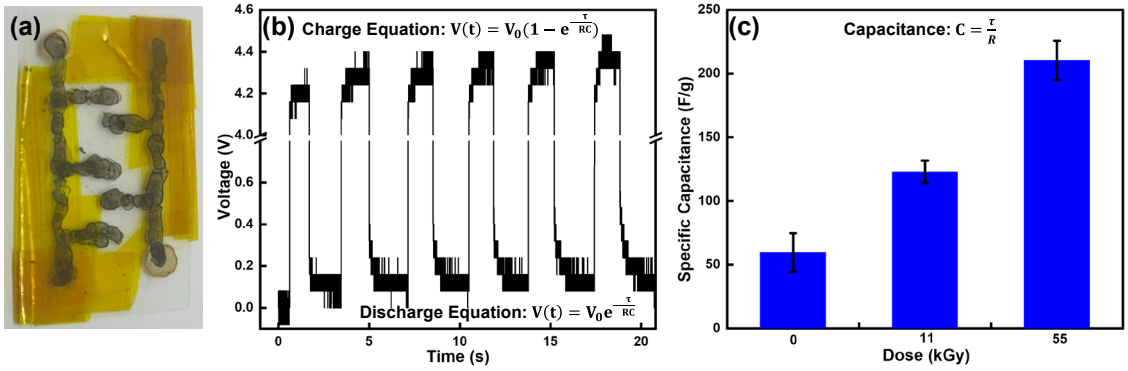

Figure 22 (a) A real image of the fabricated supercapacitor **(b)** A representative charge and discharge curve of series A (10^{-3} M) **(c)** Specific capacitances of series A before and after irradiation

4. Conclusions and Perspectives

A new approach for the one-pot synthesis of nanocomposites composed of rGO-AuNPs via gamma ray-induced radiolytic reduction has been developed in this work. Kinetic studies by UV-Vis absorption spectroscopy and spectra deconvolution demonstrated that the reduction of $[AuCl_4]^-$ is much faster, and GO is mainly reduced only after $[AuCl_4]^-$ is almost completely consumed. Structural studies by FTIR and Raman spectroscopies revealed the drastic consumption of OFGs and an increase in degree of structural disorder during irradiation. Morphological studies by SEM and AFM clearly visualized the formation of AuNPs. Elemental studies by EDX and XPS confirmed the consumption of OFGs, recovery of conjugation, and the formation of AuNPs. Thermal properties studies by TGA demonstrated the elimination of OFGs and determined the mass fraction of AuNPs in the nanocomposites. Finally, electrochemical analysis including CV and PCD demonstrated the excellent electrical properties of the synthesized nanocomposites, with enhanced specific capacitance with increase of the irradiation dose.

Future work could focus on deeper kinetic studies to calculate the rate constants using the concentration of two reducing species based on pulse-radiolysis. Additionally, investigating different concentration ratios between GO and $[AuCl_4]^-$ could help identify the optimized ratio, and stabilizer like surfactant could be introduced before irradiation to further inhibit aggregation of AuNPs. For electrochemical analysis, exploring samples at more different doses could provide further insights, and stability could be enhanced by adjusting the concentration of binder Nafion or by using different binders.

Reference

1. Geim, A. K., Graphene: status and prospects. *science* **2009,** *324* (5934), 1530-1534.

2. Geim, A. K.; Novoselov, K. S., The rise of graphene. *Nature Materials* **2007,** *6* (3), 183-191.

3. Orlita, M.; Faugeras, C.; Plochocka, P.; Neugebauer, P.; Martinez, G.; Maude, D. K.; Barra, A. L.; Sprinkle, M.; Berger, C.; de Heer, W. A.; Potemski, M., Approaching the Dirac Point in High-Mobility Multilayer Epitaxial Graphene. *Physical Review Letters* **2008,** *101* (26), 267601.

4. Balandin, A. A.; Ghosh, S.; Bao, W.; Calizo, I.; Teweldebrhan, D.; Miao, F.; Lau, C. N., Superior Thermal Conductivity of Single-Layer Graphene. *Nano Letters* **2008,** *8* (3), 902-907.

5. Lee, C.; Wei, X.; Kysar, J. W.; Hone, J., Measurement of the Elastic Properties and Intrinsic Strength of Monolayer Graphene. *Science* **2008,** *321* (5887), 385-388.

6. Novoselov, K. S.; Geim, A. K.; Morozov, S. V.; Jiang, D.; Zhang, Y.; Dubonos, S. V.; Grigorieva, I. V.; Firsov, A. A., Electric Field Effect in Atomically Thin Carbon Films. *Science* **2004,** *306* (5696), 666-669.

7. Novoselov, K. S.; Jiang, D.; Schedin, F.; Booth, T. J.; Khotkevich, V. V.; Morozov, S. V.; Geim, A. K., Two-dimensional atomic crystals. *Proceedings of the National Academy of Sciences* **2005,** *102* (30), 10451-10453.

8. Berger, C.; Song, Z.; Li, X.; Wu, X.; Brown, N.; Naud, C.; Mayou, D.; Li, T.; Hass, J.; Marchenkov, A. N.; Conrad, E. H.; First, P. N.; de Heer, W. A., Electronic Confinement and Coherence in Patterned Epitaxial Graphene. *Science* **2006,** *312* (5777), 1191-1196.

9. Choi, J.; Kim, K.-j.; Kim, B.; Lee, H.; Kim, S., Covalent Functionalization of Epitaxial Graphene by Azidotrimethylsilane. *The Journal of Physical Chemistry C* **2009,** *113* (22), 9433-9435.

10. Eizenberg, M.; Blakely, J. M., Carbon monolayer phase condensation on Ni(111). *Surface Science* **1979,** *82* (1), 228-236.

11. Kim, K. S.; Zhao, Y.; Jang, H.; Lee, S. Y.; Kim, J. M.; Kim, K. S.; Ahn, J.-H.; Kim, P.; Choi, J.-Y.; Hong, B. H., Large-scale pattern growth of graphene films for stretchable transparent electrodes. *Nature* **2009,** *457* (7230), 706-710.

12. Ismach, A.; Druzgalski, C.; Penwell, S.; Schwartzberg, A.; Zheng, M.; Javey, A.; Bokor, J.; Zhang, Y., Direct Chemical Vapor Deposition of Graphene on Dielectric Surfaces. *Nano Letters* **2010,** *10* (5), 1542-1548.

13. Compton, O. C.; Nguyen, S. T., Graphene Oxide, Highly Reduced Graphene Oxide, and Graphene: Versatile Building Blocks for Carbon-Based Materials. *Small* **2010,** *6* (6), 711-723.

14. Tarcan, R.; Todor-Boer, O.; Petrovai, I.; Leordean, C.; Astilean, S.; Botiz, I., Reduced graphene oxide today. *Journal of Materials Chemistry C* **2020,** *8* (4), 1198-1224.

15. Tan, S. M.; Ambrosi, A.; Chua, C. K.; Pumera, M., Electron transfer properties of chemically reduced graphene materials with different oxygen contents. *Journal of Materials Chemistry A* **2014,** *2* (27), 10668-10675.

16. de Barros, N. G.; Gonzaga Neto, A. C.; Vaccioli, K. B.; Angulo, H. R. V.; de Andrade e Silva, L. G.; Toffoli, S. M.; Valera, T. S., Graphene Oxide: A Comparison of Reduction Methods. *C* **2023,** *9* (3), 73.

17. Coros, M.; Pogacean, F.; Turza, A.; Dan, M.; Berghian-Grosan, C.; Pana, I.-O.; Pruneanu, S., Green synthesis, characterization and potential application of reduced graphene oxide. *Physica E: Low-dimensional Systems and Nanostructures* **2020,** *119*, 113971.

18. Capezza, A.; Andersson, R. L.; Ström, V.; Wu, Q.; Sacchi, B.; Farris, S.; Hedenqvist, M. S.; Olsson, R. T., Preparation and Comparison of Reduced Graphene Oxide and Carbon Nanotubes as Fillers in Conductive Natural Rubber for Flexible Electronics. *ACS Omega* **2019,** *4* (2), 3458-3468.

19. Ramesha, G. K.; Sampath, S., Electrochemical Reduction of Oriented Graphene Oxide Films: An in Situ Raman Spectroelectrochemical Study. *The Journal of Physical Chemistry C* **2009,** *113* (19), 7985-7989.

20. Iskandar, F.; Hikmah, U.; Stavila, E.; Aimon, A. H., Microwave-assisted reduction method under nitrogen atmosphere for synthesis and electrical conductivity improvement of reduced graphene oxide (rGO). *RSC Advances* **2017,** *7* (83), 52391-52397.

21. Zhang, Y.; Guo, L.; Wei, S.; He, Y.; Xia, H.; Chen, Q.; Sun, H.-B.; Xiao, F.-S., Direct imprinting of microcircuits on graphene oxides film by femtosecond laser reduction. *Nano Today* **2010,** *5* (1), 15-20.

22. Mao, S.; Pu, H.; Chen, J., Graphene oxide and its reduction: modeling and experimental progress. *RSC Advances* **2012,** *2* (7), 2643-2662.

23. Gao, X.; Jang, J.; Nagase, S., Hydrazine and Thermal Reduction of Graphene Oxide: Reaction Mechanisms, Product Structures, and Reaction Design. *The Journal of Physical Chemistry C* **2010,** *114* (2), 832-842.

24. Edward, I. I.; Abdul Manaf, N.; Tahir Abdul Muthalib, S. A.; Musram Rakunman, M. R.; Tan, L. S.; Tsuji, T., Synthesis of graphene oxide via electrochemical process: A short review towards flexible synthesis method. *IOP Conference Series: Materials Science and Engineering* **2021,** *1142* (1), 012019.

25. Xie, X.; Zhou, Y.; Huang, K., Advances in Microwave-Assisted Production of Reduced Graphene Oxide. *Front Chem* **2019,** *7*, 355.

26. Park, S.-H.; Kim, H.-S., Environmentally benign and facile reduction of graphene oxide by flash light irradiation. *Nanotechnology* **2015,** *26* (20), 205601.

27. Abou Zeid, S.; Bencherif, S.; Ghasemi, R.; Gogoi, R.; Chouli, Y.; Gervais, M.; Dragoe, D.; Ghilane, J.; Siril, P. F.; Remita, S., Radiation induced reduction of graphene oxide: a dose effect study. *New Journal of Chemistry* **2024,** *48* (11), 4749-4764.

28. Han, D.-D.; Zhang, Y.-L.; Liu, Y.; Liu, Y.-Q.; Jiang, H.-B.; Han, B.; Fu, X.-Y.; Ding, H.; Xu, H.-L.; Sun, H.-B., Bioinspired Graphene Actuators Prepared by Unilateral UV Irradiation of Graphene Oxide Papers. *Advanced Functional Materials* **2015,** *25* (28), 4548-4557.

29. Guo, H.; Peng, M.; Zhu, Z.; Sun, L., Preparation of reduced graphene oxide by infrared irradiation induced photothermal reduction. *Nanoscale* **2013,** *5* (19), 9040-9048.

30. Chen, L.; Xu, Z.; Li, J.; Min, C.; Liu, L.; Song, X.; Chen, G.; Meng, X., Reduction and disorder in graphene oxide induced by electron-beam irradiation. *Materials Letters* **2011,** *65* (8), 1229-1230.

31. He, Y.; Li, J.; Li, L.; Li, J., Gamma-ray irradiation-induced reduction and self-assembly of graphene oxide into three-dimensional graphene aerogel. *Materials Letters* **2016,** *177*, 76-79.

32. Fujitsuka, M.; Majima, T., Recent Approach in Radiation Chemistry toward Material and Biological Science. *The Journal of Physical Chemistry Letters* **2011,** *2* (23), 2965-2971.

33. Buxton, G., Radiation chemistry: principles and applications. *Verlag Chemie Publishers, Weinheim* **1987**.

34. Spinks, J. W.; Woods, R. J., An introduction to radiation chemistry. **1990**.

35. Henglein, A., J. W. T. Spinks. R. J. Woods: An Introduction to Radiation Chemistry, Third Edition, John-Wiley and Sons, Inc., New York, Toronto 1990. ISBN 0-471-61403-3. 574 Seiten, Preis: DM 91, 45. *Berichte der Bunsengesellschaft für physikalische Chemie* **1991,** *95* (3), 451-451.

36. Ghosh, A.; Subrahmanyam, K. S.; Krishna, K. S.; Datta, S.; Govindaraj, A.; Pati, S. K.; Rao, C. N. R., Uptake of H2 and CO2 by Graphene. *The Journal of Physical Chemistry C* **2008,** *112* (40), 15704-15707.

37. Zhou, X.; Huang, X.; Qi, X.; Wu, S.; Xue, C.; Boey, F. Y. C.; Yan, Q.; Chen, P.; Zhang, H., In Situ Synthesis of Metal Nanoparticles on Single-Layer Graphene Oxide and Reduced Graphene Oxide Surfaces. *The Journal of Physical Chemistry C* **2009,** *113* (25), 10842-10846.

38. Zhang, L.-N.; Deng, H.-H.; Lin, F.-L.; Xu, X.-W.; Weng, S.-H.; Liu, A.-L.; Lin, X.-H.; Xia, X.-H.; Chen, W., In Situ Growth of Porous Platinum Nanoparticles on Graphene Oxide for Colorimetric Detection of Cancer Cells. *Analytical Chemistry* **2014,** *86* (5), 2711-2718.

39. Kepić, D. P.; Stefanović, A. M.; Budimir, M. D.; Pavlović, V. B.; Bonasera, A.; Scopelliti, M.; Todorović-Marković, B. M., Gamma rays induced synthesis of graphene oxide/gold nanoparticle composites: structural and photothermal study. *Radiation Physics and Chemistry* **2023,** *202*.

40. Spilarewicz-Stanek, K.; Kisielewska, A.; Ginter, J.; Bałuszyńska, K.; Piwoński, I., Elucidation of the function of oxygen moieties on graphene oxide and reduced graphene oxide in the nucleation and growth of silver nanoparticles. *RSC Advances* **2016,** *6* (65), 60056-60067.

41. Kepić, D. P.; Kleut, D. N.; Marković, Z. M.; Bajuk-Bogdanović, D. V.; Pavlović, V. B.; Krmpot, A. J.; Lekić, M. M.; Jovanović, D. J.; Todorović-Marković, B. M., One-step preparation of gold nanoparticles - exfoliated graphene composite by gamma irradiation at low doses for photothermal therapy applications. *Materials Characterization* **2021,** *173*, 110944.

42. Yang, J.; Duan, X.; Guo, W.; Li, D.; Zhang, H.; Zheng, W., Electrochemical performances investigation of NiS/rGO composite as electrode material for supercapacitors. *Nano Energy* **2014,** *5*, 74-81.

43. Abou Zeid, S. Oxyde de graphène réduit et ses composites : préparation radiolytique et applications. 2023.

44. Ferradini, C.; Jay-Gerin, J.-P., The effect of pH on water radiolysis: A still open question — A minireview. *Research on Chemical Intermediates* **2000,** *26* (6), 549-565.

45. Spotheim-Maurizot, M.; Mostafavi, M.; Douki, T., *Radiation Chemistry: From Basics to Applications in Material and Life Sciences*. EDP Sciences: 2008.

46. Ferradini, C.; Jay-Gerin, J.-P., La radiolyse de l'eau et des solutions aqueuses : historique et actualité. *Canadian Journal of Chemistry* **2011,** *77*, 1542-1575.

47. Jonah, C. D., A Short History of the Radiation Chemistry of Water. *Radiation Research* **1995,** *144* (2), 141-147.

48. Draganic, Z. D.; Draganic, I. G., Formation of primary yields of hydroxyl radical and hydrated electron in the .gamma.-radiolysis of

water. *The Journal of Physical Chemistry* **1973,** *77* (6), 765-772.

49. Schwarz, H.; Dodson, R., Reduction potentials of CO2-and the alcohol radicals. *The Journal of Physical Chemistry* **1989,** *93* (1), 409-414.

50. Belloni, J., Nucleation, growth and properties of nanoclusters studied by radiation chemistry: Application to catalysis. *Catalysis Today* **2006,** *113* (3), 141-156.

51. Freitas de Freitas, L.; Varca, G. H. C.; dos Santos Batista, J. G.; Benévolo Lugão, A., An overview of the synthesis of gold nanoparticles using radiation technologies. *Nanomaterials* **2018,** *8* (11), 939.

52. PERNOT, P. *SK-Ana: Stability*, v3.4.7b; Zenodo: 2023.

53. Li, J.; Xiao, G.; Chen, C.; Li, R.; Yan, D., Superior dispersions of reduced graphene oxide synthesized by using gallic acid as a reductant and stabilizer. *Journal of Materials Chemistry A* **2013,** *1* (4), 1481-1487.

54. Paredes, J. I.; Villar-Rodil, S.; Martínez-Alonso, A.; Tascón, J. M. D., Graphene Oxide Dispersions in Organic Solvents. *Langmuir* **2008,** *24* (19), 10560-10564.

55. Gangopadhayay, A. K.; Chakravorty, A., Charge Transfer Spectra of some Gold(III) Complexes. *The Journal of Chemical Physics* **1961,** *35* (6), 2206-2209.

56. Gurunathan, S.; Han, J. W.; Eppakayala, V.; Kim, J.-H., Green synthesis of graphene and its cytotoxic effects in human breast cancer cells. *International Journal of Nanomedicine* **2013,** *8* (null), 1015-1027.

57. Kepić, D. P.; Kleut, D. N.; Marković, Z. M.; Bajuk-Bogdanović, D. V.; Pavlović, V. B.; Krmpot, A. J.; Lekić, M. M.; Jovanović, D. J.; Todorović-Marković, B. M., One-step preparation of gold nanoparticles - exfoliated graphene composite by gamma irradiation at low doses for photothermal therapy applications. *Materials Characterization* **2021,** *173*.

58. Zhang, H.; Hines, D.; Akins, D. L., Synthesis of a nanocomposite composed of reduced graphene oxide and gold nanoparticles. *Dalton Trans* **2014,** *43* (6), 2670-5.

59. Sadak, O., One-pot scalable synthesis of rGO/AuNPs nanocomposite and its application in enzymatic glucose biosensor. *Nanocomposites* **2021,** *7* (1), 44-52.

60. Maurer, T.; Nicolas, R.; Lévêque, G.; Subramanian, P.; Proust, J.; Béal, J.; Schuermans, S.; Vilcot, J. P.; Herro, Z.; Kazan, M.; Plain, J.; Boukherroub, R.; Akjouj, A.; Djafari-Rouhani, B.; Adam, P. M.; Szunerits, S., Enhancing LSPR Sensitivity of Au Gratings through Graphene Coupling to Au Film. *Plasmonics* **2014,** *9* (3), 507-512.

61. Carvalho, A. P. G.; Alegria, E. C. B. A.; Fantoni, A.; Ferraria, A. M.; do Rego, A. M. B.; Ribeiro, A. P. C., Effect of Graphene vs. Reduced Graphene Oxide in Gold Nanoparticles for Optical Biosensors—A Comparative Study. *Biosensors* **2022,** *12* (3), 163.

62. Ruckebusch, C.; Sliwa, M.; Pernot, P.; de Juan, A.; Tauler, R., Comprehensive data analysis of femtosecond transient absorption spectra: A review. *Journal of Photochemistry and Photobiology C: Photochemistry Reviews* **2012,** *13* (1), 1-27.

63. Peck, J. A.; Tait, C. D.; Swanson, B. I.; Brown, G. E., Speciation of aqueous gold(III) chlorides from ultraviolet/visible absorption and Raman/resonance Raman spectroscopies. *Geochimica et Cosmochimica Acta* **1991,** *55* (3), 671-676.

64. Szabó, T.; Berkesi, O.; Dékány, I., DRIFT study of deuterium-exchanged graphite oxide. *Carbon* **2005,** *43* (15), 3186-3189.

65. Manoratne, C.; Rosa, S.; Kottegoda, I., XRD-HTA, UV Visible, FTIR and SEM Interpretation of Reduced Graphene Oxide Synthesized from High Purity Vein Graphite. *Material Science Research India* **2017,** *14*, 19-30.

66. Mermoux, M.; Chabre, Y.; Rousseau, A., FTIR and 13C NMR study of graphite oxide. *Carbon* **1991,** *29* (3), 469-474.

67. Malard, L. M.; Pimenta, M. A.; Dresselhaus, G.; Dresselhaus, M. S., Raman spectroscopy in graphene. *Physics Reports* **2009,** *473* (5), 51-87.

68. Moon, I. K.; Lee, J.; Ruoff, R. S.; Lee, H., Reduced graphene oxide by chemical graphitization. *Nature Communications* **2010,** *1* (1), 73.

69. Ferrari, A. C.; Meyer, J. C.; Scardaci, V.; Casiraghi, C.; Lazzeri, M.; Mauri, F.; Piscanec, S.; Jiang, D.; Novoselov, K. S.; Roth, S.; Geim, A. K., Raman Spectrum of Graphene and Graphene Layers. *Physical Review Letters* **2006,** *97* (18), 187401.

70. Dai, Y.; Jing, Y.; Zeng, J.; Qi, Q.; Wang, C.; Goldfeld, D.; Xu, C.; Zheng, Y.; Sun, Y., Nanocables composed of anatase nanofibers wrapped in UV-light reduced graphene oxide and their enhancement of photoinduced electron transfer in photoanodes. *Journal of Materials Chemistry* **2011,** *21* (45), 18174-18179.

71. Boutchich, M.; Jaffré, A.; Alamarguy, D.; Alvarez, J.; Barras, A.; Tanizawa, Y.; Tero, R.; Okada, H.; Thu, T.; Kleider, J.-P. In *Characterization of graphene oxide reduced through chemical and biological processes*, Journal of Physics: Conference Series, IOP Publishing: 2013; p 012001.

72. Rozada, R.; Paredes, J. I.; Villar-Rodil, S.; Martínez-Alonso, A.; Tascón, J. M. D., Towards full repair of defects in reduced graphene oxide films by two-step graphitization. *Nano Research* **2013,** *6* (3), 216-233.

73. Tuinstra, F.; Koenig, J. L., Raman spectrum of graphite. *The Journal of chemical physics* **1970,** *53* (3), 1126-1130.

74. Zhu, C.; Guo, S.; Fang, Y.; Dong, S., Reducing Sugar: New Functional Molecules for the Green Synthesis of Graphene Nanosheets. *ACS Nano* **2010,** *4* (4), 2429-2437.

75. Stankovich, S.; Dikin, D. A.; Piner, R. D.; Kohlhaas, K. A.; Kleinhammes, A.; Jia, Y.; Wu, Y.; Nguyen, S. T.; Ruoff, R. S., Synthesis of graphene-based nanosheets via chemical reduction of exfoliated graphite oxide. *carbon* **2007,** *45* (7), 1558-1565.

76. Chua, C. K.; Pumera, M., Renewal of sp 2 bonds in graphene oxides via dehydrobromination. *Journal of Materials Chemistry* **2012,** *22* (43), 23227-23231.

77. Ossonon, B. D.; Bélanger, D., Synthesis and characterization of sulfophenyl-functionalized reduced graphene oxide sheets. *RSC advances* **2017,** *7* (44), 27224-27234.

78. Khanra, P.; Kuila, T.; Kim, N. H.; Bae, S. H.; Yu, D.-s.; Lee, J. H., Simultaneous bio-functionalization and reduction of graphene oxide by baker's yeast. *Chemical Engineering Journal* **2012,** *183*, 526-533.

79. Capezza, A.; Andersson, R. L.; Ström, V.; Wu, Q.; Sacchi, B.; Farris, S.; Hedenqvist, M. S.; Olsson, R. T., Preparation and comparison of reduced graphene oxide and carbon nanotubes as fillers in conductive natural rubber for flexible electronics. *ACS omega* **2019,** *4* (2), 3458-3468.

80. Sylvestre, J.-P.; Poulin, S.; Kabashin, A.; Meunier, M.; Luong, J. H. T., Surface Chemistry of Gold Nanoparticles Produced by Laser Ablation in Aqueous Media. *The Journal of Physical Chemistry B* **2004**.

81. Ganguly, A.; Sharma, S.; Papakonstantinou, P.; Hamilton, J., Probing the Thermal Deoxygenation of Graphene Oxide Using High-Resolution In Situ X-ray-Based Spectroscopies. *The Journal of Physical Chemistry C* **2011,** *115* (34), 17009-17019.

82. Yang, D.; Velamakanni, A.; Bozoklu, G.; Park, S.; Stoller, M.; Piner, R. D.; Stankovich, S.; Jung, I.; Field, D. A.; Ventrice, C. A.; Ruoff, R. S., Chemical analysis of graphene oxide films after heat and chemical treatments by X-ray photoelectron and Micro-Raman spectroscopy. *Carbon* **2009,** *47* (1), 145-152.

83. Park, S.; Ruoff, R. S., Chemical methods for the production of graphenes. *Nature Nanotechnology* **2009,** *4* (4), 217-224.

84. Deng, S.; Berry, V., Wrinkled, rippled and crumpled graphene: an overview of formation mechanism, electronic properties, and applications. *Materials Today* **2016,** *19* (4), 197-212.

85. Alam, S. N.; Sharma, N.; Kumar, L., Synthesis of graphene oxide (GO) by modified hummers method and its thermal reduction to obtain reduced graphene oxide (rGO). *Graphene* **2017,** *6* (1), 1-18.

86. Malas, A.; Das, C. K.; Das, A.; Heinrich, G., Development of expanded graphite filled natural rubber vulcanizates in presence and absence of carbon black: Mechanical, thermal and morphological properties. *Materials & Design* **2012,** *39*, 410-417.

87. Jelen, Ž.; Krajewski, M.; Zupanič, F.; Majerič, P.; Švarc, T.; Anžel, I.; Ekar, J.; Liou, S.-C.; Kubacki, J.; Tokarczyk, M.; Rudolf, R., Melting point of dried gold nanoparticles prepared with ultrasonic spray pyrolysis and lyophilisation. *Nanotechnology Reviews* **2023,** *12* (1).

88. Jayachandiran, J.; Yesuraj, J.; Arivanandhan, M.; Raja, A.; Suthanthiraraj, S. A.; Jayavel, R.; Nedumaran, D., Synthesis and electrochemical studies of rGO/ZnO nanocomposite for supercapacitor application. *Journal of Inorganic and Organometallic Polymers and Materials* **2018,** *28*, 2046-2055.

89. Saravanan, T.; Shanmugam, M.; Anandan, P.; Azhagurajan, M.; Pazhanivel, K.; Arivanandhan, M.; Hayakawa, Y.; Jayavel, R., Facile synthesis of graphene-CeO2 nanocomposites with enhanced electrochemical properties for supercapacitors. *Dalton Transactions* **2015,** *44* (21), 9901-9908.

90. Stoller, M. D.; Park, S.; Zhu, Y.; An, J.; Ruoff, R. S., Graphene-based ultracapacitors. *Nano letters* **2008,** *8* (10), 3498-3502.

91. Krishnan, P.; Biju, V., Effect of electrolyte concentration on the electrochemical performance of RGO–KOH supercapacitor. *Bulletin of Materials Science* **2021,** *44* (4), 288.

92. Yang, J.; Gunasekaran, S., Electrochemically reduced graphene oxide sheets for use in high performance supercapacitors. *Carbon* **2013,** *51*, 36-44.

93. Vivekchand, S.; Rout, C. S.; Subrahmanyam, K.; Govindaraj, A.; Rao, C. N. R., Graphene-based electrochemical supercapacitors. *Journal of Chemical Sciences* **2008,** *120*, 9-13.

94. El-Kady, M. F.; Strong, V.; Dubin, S.; Kaner, R. B., Laser Scribing of High-Performance and Flexible Graphene-Based Electrochemical Capacitors. *Science* **2012,** *335* (6074), 1326-1330.